UNIVERSITY OF CALIFORNIA SAN DIEGO

Interannual Variability of Sea Ice Area and Volume in the Greenland Sea

A thesis submitted in partial satisfaction of the requirements for the degree Master of Science

in

Oceanography

by

Alex R. Hamel

Committee in charge:

Professor Fiammetta Straneo, Chair
Professor Ian Eisenman
Professor Helen Amanda Fricker
Professor Lars Henrik Smedsrud

2020

The thesis of Alex R. Hamel is approved, and it is acceptable in quality and form for publication on microfilm and electronically:

_____

_____

_____

_____
Chair

University of California San Diego

2020

TABLE OF CONTENTS

Signature Page…… iii

Table of Contents…… iv

List of Abbreviations……. vi

List of Figures……...…….. viii

List of Tables……... x

Acknowledgements……. xi

Abstract of the Thesis…….. xii

Chapter 1: Introduction..……...…… 1

1.1 Aims and Objectives……. 1

1.2 Background……..……. 2

1.2.1 Importance of Sea Ice in a Changing Climate….……. 2

1.2.2 Prior Studies…..……..…. 4

1.2.3 Regional Characteristics…….…..……. 6

1.2.4 Bathymetry…….…..……. 7

1.2.5 Physical Processes……..…..……. 8

Chapter 2: Data and Methods..……..……. 10

2.1 Data…….……. 10

2.1.1 Data Set Selection…… 10

2.1.2 Sea Ice Concentration…….. 10

2.1.3 Sea Ice Displacement Vectors……. 14

2.1.4 Sea Ice Thickness Estimates...……. 16

2.1.5 Radiative Fluxes……..……. 16

2.2 Methods..…….……. 17

2.2.1 Sea Ice Area Trends……...……. 17

2.2.2 Sea Ice Area Transport……..……. 18

2.2.3 Thickness……..…….. 22

2.2.4 Volume Transport……..……..…….. 22

2.2.5 Volume Budget……..……. 23

2.2.6 Heat Fluxes……..……... 24

Chapter 3: Results..……..…….. 26

3.1 Sea Ice Area…….……. 26

3.1.1 Study Area Trends……..……. 26

3.1.2 Loss of the Odden Ice Tongue……. 28

3.1.3 Effect of the Odden Ice Tongue on the Winter Maximum 31

3.1.4 Sea Ice Area Transport……..……. 32

3.2 Sea Ice Thickness…….…… 33

3.3 Volume Transport…….…… 35

3.4 Volume Budget…….…… 38

3.4.1 Seasonal Change……... 38

3.4.2 Odden Ice Tongue Contribution…… 39

Chapter 4: Discussion..……..…….… 42

4.1 Errors and Uncertainty…….. 42

4.2 Comparison to Similar Results..……... 45

4.3 Warming Atlantic…….. 47

Chapter 5: Conclusion…….… 49

5.1 Conclusions……... 49

5.2 Future Work…….. 51

References…… 52

LIST OF ABBREVIATIONS

AVHRR - Advanced Very High-Resolution Radiometer

AW – Atlantic Water

^{o}C – Degrees Celsius

CERSAT - Centre ERS d'Archivage et de Traitement

DMSP – Defense Meteorological Satellite Program

EASE - Equal Area Scalable Earth

ECMWF - European Centre for Medium-Range Weather Forecasts

EGC – East Greenland Current

ERA5 - ECMWF reanalysis iteration 5

EUMETSAT - European Organisation for the Exploitation of Meteorological Satellites

IABP – International Arctic Buoy Program

IPCC - Intergovernmental Panel on Climate Change

ITP – Ice-Tethered Profiler

Km - Kilometers

m – Meters

m/s – Meters per second

NAC – North Atlantic Current

NAO – North Atlantic Oscillation

NASA - National Aeronautics and Space Administration

NCAR - National Center for Atmospheric Research

NCEP - National Center for Environmental Prediction

NOAA - National Oceanic and Atmospheric Administration

NorESM – Norwegian Earth System Model

NSIDC - National Snow and Ice Data Center

OSI SAF - Ocean and Sea Ice Satellite Application Facility

PIOMAS - Pan-Arctic Ice-Ocean Modeling and Assimilation System

SMMR - Scanning Multichannel Microwave Radiometer

SSM/I - Special Sensor Microwave/Imager

SSMIS - Special Sensor Microwave Imager/Sounder

SST – Sea surface temperature

WHOI - Woods Hole Oceanographic Institution

W/m^2 – Watts per square meter

LIST OF FIGURES

Figure 1: Study area…….. 2

Figure 2: North and south divisions of study area…… 6

Figure 3: Seafloor bathymetry…….. 7

Figure 4: Sea ice area transport (Smedsrud et al. 2017)……... 8

Figure 5: Prevailing ocean currents in the study area (WHOI)…… 9

Figure 6: Comparison of NASA Team and Bootstrap algorithms…… 11

Figure 7: Sea ice concentration on NSIDC polar stereographic projection…….. 12
(Tschudi et al. 2019 and Peng et al. 2013)

Figure 8: Polar Pathfinder sea ice vectors on Equal Area Scalable Earth grid……. 13

Figure 9: Mean velocity across (a) the Fram Strait (southward component) and…… 18
(b) the Denmark Strait (perpendicular component).

Figure 10: Geometry of sea ice motion across the Denmark Strait…… 19

Figure 11: Time series of sea ice area in the north and south boxes…….. 24

Figure 12: Summer and winter trends in sea ice area separated by box……. 25

Figure 13: Example of Odden Ice Tongue development (Comiso et al. 2001)……... 26

Figure 14: Sea ice area trends in north box and on the continental shelf and…… 28
influence of the Odden Ice Tongue

Figure 15: Average annual cycle of sea ice area from 1979-2018 ……. 29
in 5-year bins

Figure 16: Annual sea ice area flux across Fram Strait and Denmark Strait…….……. 30

Figure 17: PIOMAS sea ice thickness across Fram Strait and Denmark Strait…….. 32

Figure 18: Mean annual cycle of sea ice draft across Fram Strait……. 33
for 1979-2004 and 2005-2018.

Figure 19: Sea ice volume transport across Fram Strait and Denmark Strait…… 34

Figure 20: Seasonally integrated volume transport for Denmark Strait and ……. 35
Fram Strait from September through March

Figure 21: Annual cycle of sea ice volume in the north box pre and post 2004……. 36

Figure 22: Volume of each Odden Ice Tongue over the course of the record……. 38

Figure 23: Sea ice concentration in the north box and ……. 46
sea surface temperature west of Norway

LIST OF TABLES

Table 1: Geographic locations of points spaced at 25km across the Fram…… 20
and Denmark Straits

Table 2: Geographic locations of points spaced at 21km across the Fram…… 22
and Denmark Straits

Table 3: Volume budget for north box…….. 39

Table 4: Known uncertainties for included data sets……. 42

ACKNOWLEDGMENTS

First to my cohort members in CASPO and the Local Support Group – Alex, Athina, Duncan, Bethan, Deb, Cassandra, Yuming, Philip, Cody, Pascal, Alli, Anne, and Max - it would have been a different experience without you. I think about that good fortune a lot, and when I look back on my time Scripps it will be on you guys.

To my advisor, Fiamma, who showed me patience when I didn't deserve it and who often knew what I needed before I did. You taught me more than science, and I predict those lessons will stick with me the most.

To Lars Henrick, who could have used his time away from Norway in likely more fruitful endeavors, but nevertheless chose to spend some of it with me.

To Bobby, Margaret, Jamie, Isi, and Donald (top lad), and the rest of the Ice/Ocean group. I couldn't have asked for a better team.

This thesis, in part is currently being prepared for submission for publication of the material. Straneo, Fiammetta; Smedsrud, Lars H. The thesis author was the primary investigator and author of this material.

ABSTRACT OF THE THESIS

Interannual Variability of Sea Ice Area and Volume in the Greenland Sea

by

Alex R. Hamel

Master of Science in Oceanography

University of California San Diego, 2020

Professor Fiammetta Straneo, Chair

Arctic sea ice loss continues to serve as a strong gauge of climate change. It is the component of the Earth system that is responding most visibly and rapidly to a warming climate. The implications of a shrinking sea ice cover include changes in physical processes like deep water formation and the reflection of solar radiation, and alterations to the way of live for humans and animals that depend on the ice in their daily lives. Here I evaluate long term trends in sea ice coverage in the Greenland Sea and Irminger Basin from 1979 to 2018. While in the Arctic Basin the recession of summer sea ice is more pronounced, it is shown that in the Greenland Sea the declining winter sea ice maximum is more pronounced than the summertime reduction. The strongest signature

of this robust trend is the disappearance in 2004 of a sea ice feature called the Odden Ice Tongue that is characterized by local freezing and ice formation and to a lesser extent by the advection of sea ice. A budget constructed from sea ice concentration and velocity estimates from the National Snow and Ice Data Center, and sea ice thickness estimates from the University of Washington's Pan-Arctic Ice Ocean Modeling and Assimilation System indicates that the area of sea ice transported into the Greenland Sea from the Arctic has gone largely unchanged since measurements began in late 1978. Despite this, the volume of sea ice flowing out of the Arctic has decreased 11% when compared to the 1979-2004 mean due to a significant thinning of sea ice.

In the last 15 years the average winter buildup of sea ice volume in the Greenland Sea is 16% smaller than the same winter accumulation from 1979 to 2004. The volume of sea ice that is advected into the Greenland Sea, from Fram Strait, is approximately twice as large as the change in volume of sea ice in the area over the course of a typical winter, indicating that half of the advected sea ice melts over the course of the winter.

CHAPTER 1: INTRODUCTION

1.1 Aims and Objectives

The goal of this research was to better understand the cycle of sea ice advance and retreat along the east coast of Greenland and the Greenland Sea. The movement of sea ice has profound implications on high latitude physical processes, namely fresh water transport, deep water formation, changes in surface albedo, and surface heat fluxes. The cadence of the interannual cycle of sea ice is a significant social variable as well. In the case of this study, settlements on the east coast of Greenland rely on the sea ice for hunting and transportation, and communities around the entire Arctic are likewise inescapably tied to the movement of the ice. No single variable was the motivation for conducting the study, but rather to better understand the cycle of the freezing, melting, and transport of sea ice.

Figure 1 depicts a broad view of the study area. Satellite observations and numerical simulations from publicly available sources were used to examine the area or "extent" of sea ice, as well as changes in thickness, volume, and transport of sea ice in the study area from 1979 through 2018. This time frame was chosen based on the availability of satellite data beginning in late 1978. Data sets are discussed in further detail in Chapter 2. The specific goals of this study were to:

1) Establish the sea ice volume budget for East Greenland.
2) Examine trends in the interannual variability of sea ice area and volume for East Greenland.

This study was highly motivated by the results presented in Onarheim et al. (2018) that included characterizations of the seasonal loss of sea ice in different regions of the Arctic. Here I examine the Greenland Sea and continental shelf in more detail.

Figure 1. *Study area on the east side of Greenland (National Oceanic and Atmospheric Administration General Bathymetric Chart of the Oceans).*

1.2 Background

1.2.1 Importance of Sea Ice in a Changing Climate

The loss of Arctic sea ice is a well-documented and widely-familiar topic in the context of a changing climate. This decline of sea ice persists as a reliable telltale of warming trends on local, regional, and global scales. Despite observing this common signal, different areas of the Arctic experience sea ice loss at different rates, different times, and for different reasons. Despite this inhomogeneous nature of the Arctic Ocean and its surrounding seas, ice loss is distinctly visible in all regions in the Arctic throughout the year (Onarheim et al. 2018). The Greenland Sea is no exception to this trend. This region of the Arctic has continuously experienced a decline in sea ice coverage,

especially during the coldest winter months, since satellite observations first began in 1978 (Onarheim et al. 2018).

The role of sea ice through the lens of a larger climate perspective is different than that of icebergs, glaciers, ice shelves, and other components of earth's cryosphere. Glaciers, icebergs, and large ice shelves (most recognizable in the margins of the Antarctic continent) originate on land and flow into the sea, but sea ice forms on the ocean and is a floating layer of frozen ocean water. Sea ice is highly reflective, and the frozen poles of the planet are responsible for reflecting a large fraction (Pistone et al. 2019) of incoming solar radiation away from the surface (albedo). The self-perpetuating loop of melting sea ice, less reflection, more absorbed radiation, warming waters, and therefore more melting ice is known as the ice-albedo feedback, and is frequently cited as a major contributor to a changing climate due to increased carbon dioxide levels in the atmosphere (Stroeve and Notz 2018).

Sea ice formation at the surface also controls physical processes down to the depths of deepest oceans. As sea ice forms, salt molecules that are not compatible with the chemical structure of ice are left behind. The salt rejected as sea ice freezes creates brine that is saltier, and therefore denser, than the surrounding sea water. This denser water sinks to the bottom, and accumulates to form the deep water masses that circulate the globe (Talley et al. 2011). This process is called "brine rejection", and has profound implications on overturning circulation from the poles to the deep global ocean water masses.

Ice cover also significantly reduces heat, light, and nutrient exchange between the ocean and the atmosphere. One meter of ice will almost totally insulate the ocean (Talley el a. 2011), and reducing that insulating cover means more heat from the sun (and carbon from the atmosphere) is absorbed by the ocean.

Sea ice extent directly controls the size of habitats and hunting ground for marine mammals like sea lions, seals, and polar bears, and therefore humans as well. Communities around the Arctic rely on what was once a predictable cadence of sea ice advance and retreat to hunt and travel. As the sea ice melts, the usable habitat for animals and humans wanes with it.

Conversely, where local communities are faced with the compounding challenges of melting sea ice, commercial industries see opportunity. Areas once inaccessible due to the perpetual and formidable blockade of a sea ice barrier are now ice-free for the summer season, while some are on track to be completely ice-free year-round (Onarheim et al. 2018, Stroeve and Notz 2018). The Bering Sea and Sea of Okhotsk are examples of such a trend. Natural resource exploration, tourism, and changing shipping routes are all industries now in the public eye where there were no such opportunities existed before the onset of an era where humans have increasingly influenced the trajectory of our natural surroundings.

1.2.2 Prior Studies

Sea ice extent has been declining on an Arctic-wide scale since satellite measurements began largely due to the warming atmosphere related to the input of carbon dioxide into the atmosphere from anthropogenic sources (Stroeve and Notz 2018). Recent studies have taken to more nuanced approaches of evaluating regional and seasonal changes and the drivers behind them (i.e. changes in winter sea ice cover versus summer sea ice cover in the Bering Sea). Onarheim et al. (2018) examined trends on both an Arctic-wide scale and regionally by using areas defined by the National Snow and Ice Data Center (NSIDC). That 2018 study found that the Greenland Sea is experiencing a disproportional loss of sea ice in the winter months, with the area contributing about 25% of Arctic-wide sea ice loss in the month of March (typical timing of winter sea ice maximum).

Sea ice export from the Arctic is of great relevance as well. Using methods that included Synthetic Aperture Radar (SAR) image analysis and investigation of mean sea level pressure gradients and associated geostrophic winds, two studies by Smedsrud et al. (2008 and 2016) found no long-term trends in sea ice area export from the Arctic into the Greenland Sea for separate time periods between 1935 and 2014, but also an increasing trend in area export over the length of the satellite observation era, especially during spring. Similarly, Zamani et al. (2019) showed a positive trend in monthly sea ice area export between the Arctic and Greenland Sea from 1990 to 2010.

Changes in sea ice thickness are a challenging to estimate and observe. Smedsrud et al. in 2016 found a general thinning of sea ice in the study area after 2000 using airborne electromagnetic measurements, and Hansen et al. (2013) used moored sonars to show a thinning from 1990-2011. Ricker et al. (2018) investigated ice volume transport through the Fram Strait using CryoSat-2 thickness retrievals and found that the seasonal trend in volume export is driven by ice thickness, however both Ricker et al. (2018) and Zamani et al. (2019) found no significant trend in volume export during their respective study periods (2010-2017 and 1990-2010).

A warming Atlantic is also well documented. Spielhagen et al. (2011), Levitus et al. (2019), and Muilwijk et al. (2018) present results supporting increased heat transport from the North Atlantic Ocean to the Arctic. Most relevantly, Onarheim et al. (2014) presented an accountability of sea ice loss north of Svalbard with an increase in Atlantic water temperature entering the region since 1979.

To summarize, the Greenland Sea is experiencing a reduction in sea ice cover, an increase or stagnation in sea ice area export from the Arctic, a reduction in sea ice thickness, and an increase in the temperature of Atlantic water entering the area. However previous studies have not computed the annual mean budget of sea ice growth and decay for the Greenland Sea, nor has the volume of sea ice decline been estimated for the time period investigated here.

1.2.3 Regional Characteristics

The area of interest for this study is the east continental shelf of Greenland and the Greenland Sea (Figure 1). This investigation used standard data products provided by the National Snow and Ice Data Center, which specializes in remote sensing of the cryosphere with support from the National Aeronautics and Space Administration (NASA), the National Oceanic and Atmospheric Administration (NOAA), and the National Science Foundation (NSF). The NSIDC defines a "Greenland Sea" region (National Snow and Ice Data Center 2010), which in this case was further refined to better conform/compare to existing studies in the region. Figure 2 depicts the bounds of the study area compared to the NSIDC-defined region. The area is more explicitly defined as that bounded to the north by the Fram Strait between Greenland and Svalbard at 79°N, and to the south by Cape Farewell, Greenland at 59.5°N. The western boundary is the Greenland continent, and the eastern boundary is constrained by the west coast of Svalbard from 79°N to 76.5°N, the east coast of Iceland at 66.5°N, and rhumb lines connecting those points to Cape Farewell. The study area was

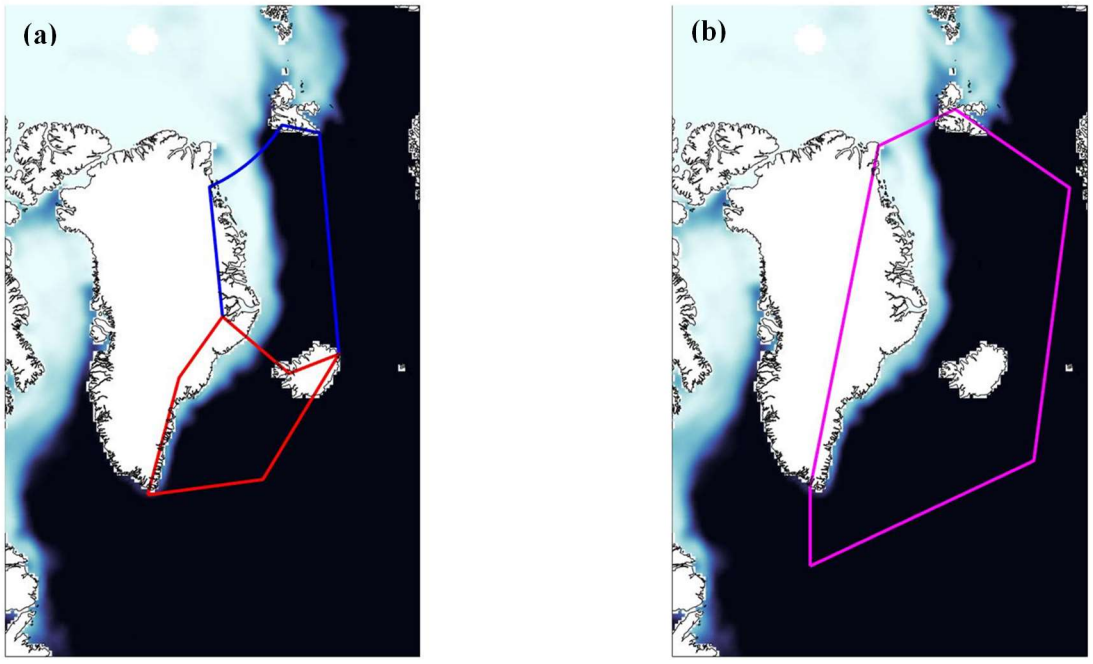

Figure 2. *(a) North and south boxes as defined for this study. (b) National Snow and Ice Data Center region 7 – Greenland.*

then further separated into north and south “boxes” using the Denmark Strait between Iceland and Greenland as a demarcation line. The exact endpoints of the line were selected based on the location of an existing mooring array from the Woods Hole Oceanographic Institution (WHOI) Kögur Project. This Kögur section array is used to quantify pathways of currents and circulation in the Denmark Strait (de Steur et al. 2017, Våge et al. 2013) and also transects the narrowest point of the Strait.

1.2.4 Bathymetry

In addition to north and south separations, the study area was further divided in two distinct zones based on sea floor bathymetry. A relatively shallow shelf with a depth of less than 500 m

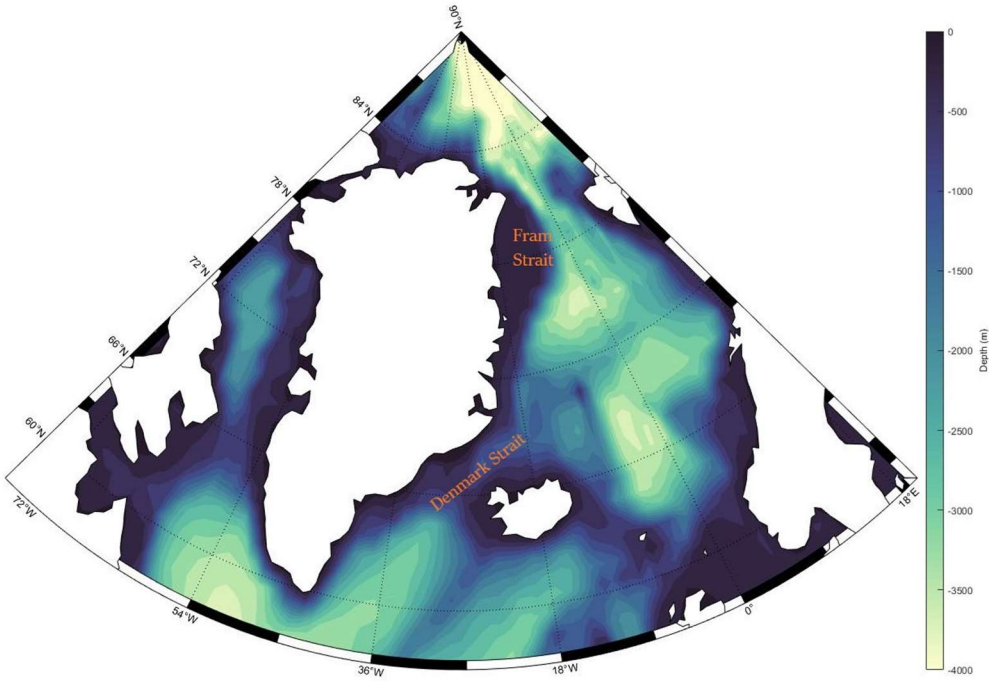

Figure 3. *Seafloor bathymetry in the study area.*

extends approximately 200-300 km from the Greenland and Iceland continents. The shelf slopes sharply into the basin of the Greenland Sea to a maximum depth of approximately 3,000 m (figure 3). The Denmark Strait is narrow enough (400 km) to see the continental shelves of Iceland and

Greenland converge to create a shallower "sill" when viewed on the scale of the entire region with a depth of approximately 350 m.

1.2.5 Physical Processes

Sea ice variability in the study area is a function of several physical processes, the most prominent of which is transport (advection) through the Fram Strait. Like water, the movement of ice floating on top of it is subject to ocean currents, wind, and major storm events. While some sea ice does form locally each year, approximately 10% of the Arctic's sea ice flows into the Greenland Sea

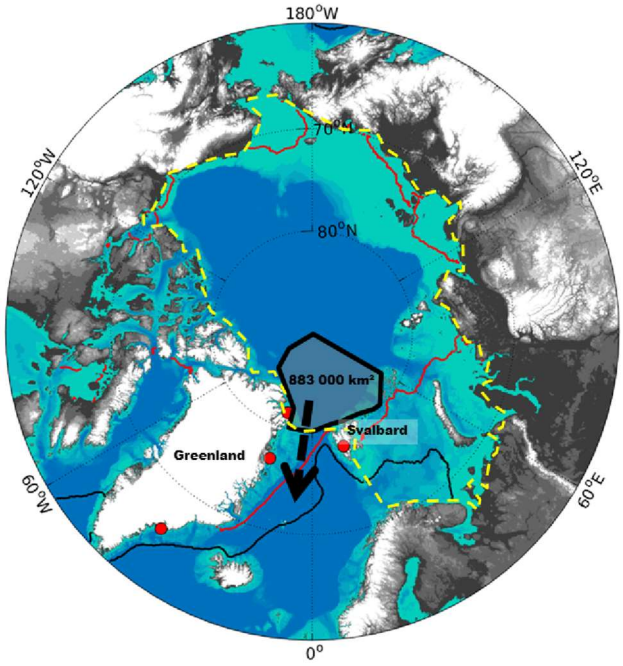

Figure 4. *Area transport of ice through the Fram Strait (Smedsrud et al. 2017)*

annually (Smedsrud et al. 2016, Zamani et al. 2019), which is an area value of almost 1 million km^2 of sea ice. The ocean current that carries the ice through Fram Strait is the East Greenland Current (EGC), and is part of the network of ocean currents depicted in figure 5 that stem from the North Atlantic Current (NAC). The heat that these currents carry from subtropical and tropical latitudes to the Atlantic Ocean may be the second major process controlling sea ice in the Greenland Sea

(Muilwijk et al. 2018). The NAC is the primary culprit in this sense, as it acts as an extension of the Gulf Stream carrying warmer waters from the tropical Atlantic all the way to the Arctic.

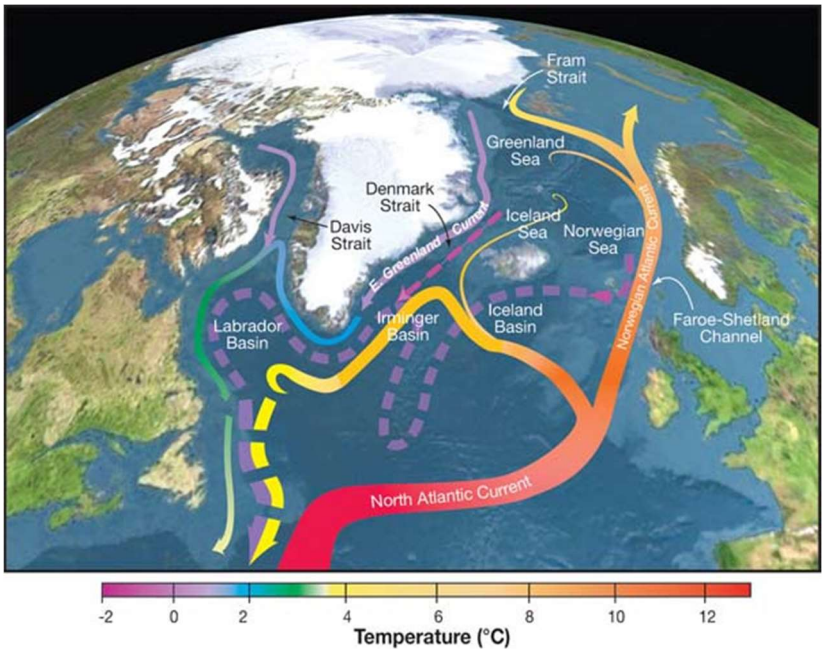

Figure 5. *Prevailing ocean currents in the study area (Woods Hole Oceanographic Institution)*

CHAPTER 2: DATA AND METHODS

2.1 Data

2.1.1 Data Set Selection

The three primary data sources relied on for this study were the NSIDC Passive Microwave Sea Ice Concentration data set, the NSIDC Polar Pathfinder Ice Motion Vectors, and the PIOMAS model output from the University of Washington. It should be noted that the PIOMAS model output includes sea ice thickness, concentration, and velocity (among other variables) by itself, and this study could have reasonably been completed using only those data sets. However, I decided to minimize reliance on modeled values. The NSIDC data sets are both observational. Taking this approach allowed for completing the volume budget analysis for the length of the satellite era (1978-present) while minimizing dependence on modeled values and maximizing consistency between data sets (the two NSIDC data sets both rely on the NASA Team sea ice concentration algorithm).

2.1.2 Sea Ice Concentration

Beginning with the NASA Nimbus-7 mission in November 1978 and continuing through four iterations of the Defense Meteorological Satellite Program (DMSP) up to the current day, satellite passive microwave data has become the standard for observing and interpreting changes in sea ice and other components of the cryosphere. Following the initial launch of the Nimbus-7 satellite equipped with a Scanning Multichannel Microwave Radiometer (SMMR) in 1978, the Defense Meteorological Satellite Program (DMSP) began recording satellite data in 1987. A Special Sensor Microwave/Imager (SSM/I) was implemented and routinely updated three times in 1987, 1991, and 1995, and stayed in service until 2008 when data from the Special Sensor

Microwave Imager/Sounder (SSMIS) superseded the SSM/I and is currently still in use today. This technology provides a continuous 40-year record that is relied on by scientists worldwide. Published results that utilize these data have been included in the United Nations Intergovernmental Panel on Climate Change (IPCC) as cited in their most recent reports in 2007 (IPCC AR4) (IPCC, 2007) and 2013 (IPCC AR5) (IPCC, 2013).

Microwave radiometers and imagers aboard these NASA and Department of Defense satellites make passive measurements of spectral radiance at the surface based on microwave blackbody radiation of different materials. This is called the brightness temperature, which is linearly related to the kinetic temperature of the surface. This linear approximation provides a simple relationship between the measured spectral radiance temperature and emissivity, where emissivity is the ability of a material (i.e. ice, seawater, rock) to emit radiation. The ability of passive microwave data to be able to detect the presence of sea ice is due to the high contrast between the emissivity of open water and sea ice (Cavalieri et al. 1984), and it is also insensitive to day/night conditions.

The satellites have an orbital period of 101 to 104 minutes and provide global coverage twice per day with the exception of a small circular sector over the North Pole due to the orbit inclination of the satellite. The SMMR, SSM/I, and SSMIS sensors were/are limited to coverage below 84.5^{o}N, 87.2^{o}N, and 89.18^{o}N respectively. Data are averaged daily between the two passes, and then averaged over each month to create a monthly composite image allowing for both daily and monthly resolution products.

There are two widely used algorithms used to create gridded sea ice concentration data from the microwave radiances received by the spacecraft, both of which were developed at NASA Goddard Space center: The "NASA Team" algorithm, as described in Cavalieri et al. (1984), and the "Bootstrap" algorithm as described in Comiso (1986). The NASA Team algorithm relies on ratios of brightness temperature estimates from different channels in the microwave region, while the Bootstrap method interpolates sea ice concentration between clusters of known ice types (first year versus multi-year ice). Figure 6 depicts a comparison between the two algorithms in the form of a time series of sea ice area in the north box of the study area. The two methods have their own advantages and disadvantages, but are nonetheless quite statistically similar in the region of interest (R=0.99). The method behind constructing these time series is discussed in section two of this chapter.

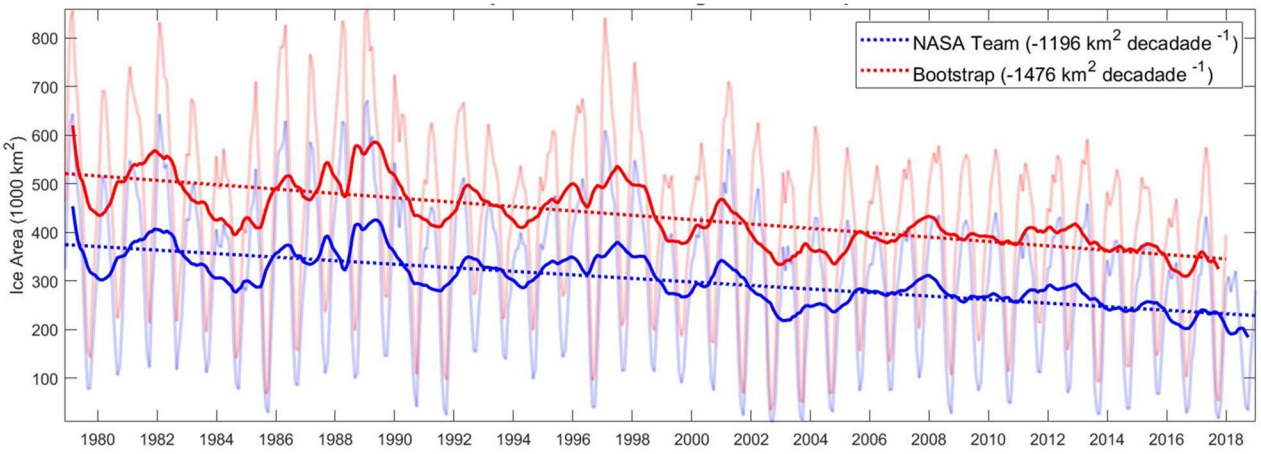

Figure 6. *Comparison of sea ice area results in the north box using NASA Team and Bootstrap algorithms. Trends are significant to 95% confidence.*

Some documented weaknesses of the NASA Team algorithm include that it underestimates the concentration of thin sea ice, and that errors are higher in regions where melting and refreezing occurs. Shortcomings of the Bootstrap algorithm include sensitivity to changes in temperature which has implications for estimating the concentration of thin sea ice, and high errors in very cold regions (NSIDC). Each method grids the data onto the 25 km x 25 km NSIDC polar stereographic north projection, which has its projection plane to the Earth's surface set at 70° N. Figure 7.a is an example of a daily sea ice image on a polar stereographic projection. A typical polar projection map is centered at the north or south pole, however in this case, changing the reference latitude allows for the minimal distortion of grid cells in the marginal sea ice zone, or "ice edge," where sea ice concentration changes the most frequently and the most strongly. Minimizing cell distortion directly at the north pole is far less useful since

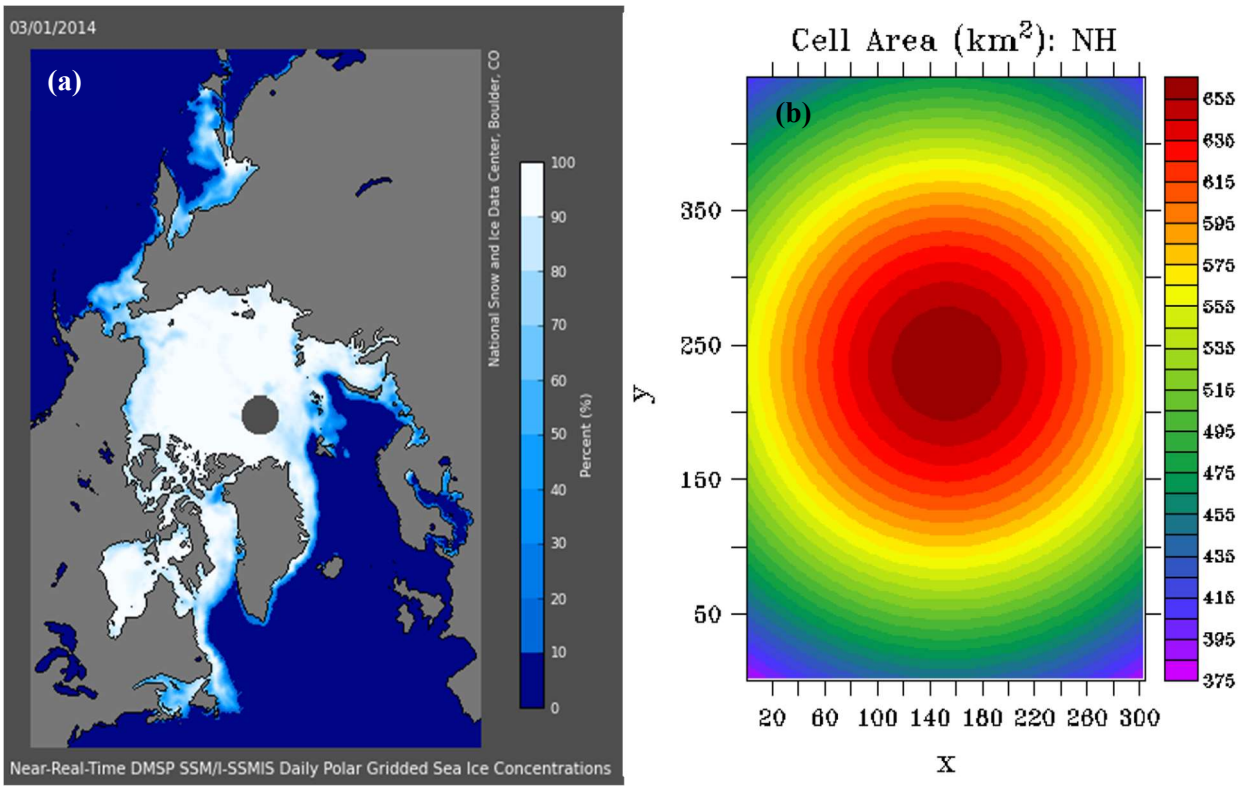

Figure 7. *(a) Passive microwave sea ice concentration, March 1st 2014 (National Snow and Ice Data Center). (b) Cell area by latitude of (a) from Peng et al.2013. Nominal resolution is 625 km² .*

it is consistently measured at 100% sea ice concentration. Figure 7.b shows the cell distortion of the Polar Stereographic grid as a function of latitude. For the purposes of this study, the NASA Team algorithm was selected in order to better coincide with the sea ice motion data product described below.

2.1.3 Sea Ice Displacement Vectors

Daily and weekly sea ice motion vectors are also provided from the NSIDC based on several inputs from satellite and in situ measurements. The Polar Pathfinder Equal Area Scalable Earth (EASE) Grid Sea Ice Motion Vectors (Tschudi et al. 2019; figure 8) compile inputs from multiple sources, most notably the passive microwave sea ice concentration data described above utilizing the NASA Team algorithm. The results are gridded on to the 25 km x 25 km EASE grid that does not vary from its nominal resolution like the Polar Stereographic projection. Other input sources include visual and infrared images collected by the Advanced Very High

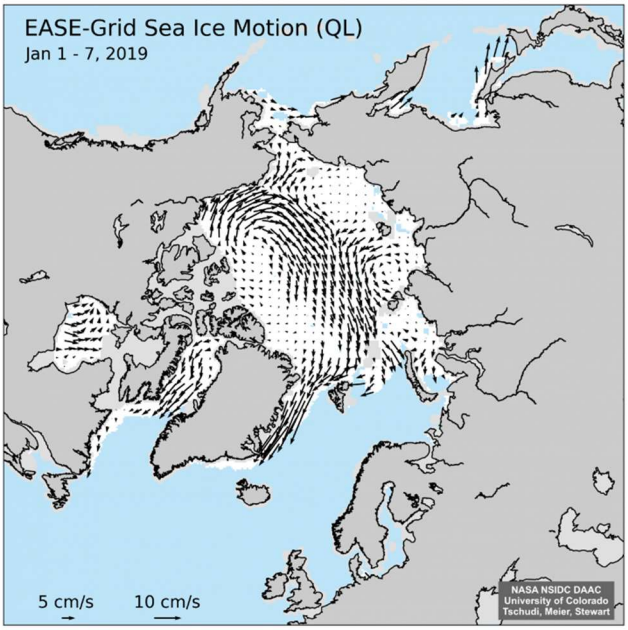

Figure 8. *Polar pathfinder weekly average sea ice motion, January 1-7, 2019 (NSIDC).*

Resolution Radiometers (AVHRR) aboard the NOAA Polar Orbiting Environmental Satellites, position data collected by the International Arctic Buoy Program (IABP), and 10-meter wind velocities from the National Center for Environmental Prediction and National Center for Atmospheric Research (NCEP/NCAR) climate reanalysis data set. Daily estimates of ice motion are averaged into weekly products (figure 8).

Sea ice motion can be manually computed from measuring the displacement between a distinct feature (iceberg or ice floe) in consecutive images. A more automated approach is used in this dataset that measures the correlation of groups of pixels between image pairs. As defined by the Polar Pathfinder documentation, a small target area in one image is correlated with several areas of the same size in a search region of the second image. The displacement vector is then defined by the location in the second image where the correlation coefficient is the highest. This is accomplished using the passive microwave data and the high-resolution images in both visual and infrared spectra.

Cloud cover and changes in surface temperature can make these visual and infrared measurements unreliable, especially during the summer when the surface water temperature is similar to the ice temperature, so this method is augmented by motion estimates from buoys in the sea ice and climate reanalysis wind vectors. Buoy data is sparse, but most accurate, followed in decreasing accuracy by vectors derived from satellite image analysis, and then finally by wind analysis. Wind-derived motion is the least accurate because it is input from a climate model that very loosely approximates the relationship between sea ice and wind (Thorndike et al 1982) versus the direct buoy and satellite observations. Ocean currents also offset the wind-based speed estimates.

The final sea ice motion product is a result of weighting the input sources (microwave, visual, infrared, wind) based on cross-correlations with buoy vectors (Tschudi et al 2019).

2.1.4 Sea Ice Thickness Estimates

An Arctic-scale observational data set of thickness does not exist over the length of the entire study period. For the purpose of estimating sea ice volume transport, which requires a thickness variable on the spatial and temporal scales examined here, I relied on the Pan-Arctic Ice-Ocean Modeling and Assimilation System (PIOMAS) model from the Applied Physics Laboratory at the University of Washington (Zhang and Rothrock 2003). PIOMAS is a coupled ocean and sea ice model with 15 output variables. The only output from PIOMAS used for this study was sea ice thickness. The sea ice model is driven by atmospheric forcing (surface winds, temperature, radiative fluxes, precipitation/evaporation, humidity), which in turn supplies surface heat, salt, and momentum fluxes to the ocean. The ocean model then supplies current and heat information to the sea ice model. A 360 x 120 generalized curvilinear coordinate system from 45^{o}N to 95^{o}N is the grid configuration for the output fields, but latitude and longitude points do change between vector and scalar outputs. Values are provided monthly.

2.1.5 Radiative Fluxes

The European Centre for Medium-Range Weather Forecasts (ECMWF) provides a climate reanalysis data set useful for calculating changes in sea surface temperature and radiation fluxes from 1950-present (Copernicus Climate Change Services 2017). The ECMWF reanalysis (ERA) is a large and highly complex product with global 3D spatial coverage and sub-daily

temporal resolution. The fifth version of the reanalysis, ERA5, was utilized to consider sea surface temperature, short wave (incoming) radiative fluxes, long wave (outgoing) radiative fluxes, and latent heat flux at the surface at monthly resolution. Output variables are gridded to a reduced Guassian grid, which evenly distributes data points along each parallel but irregularly distributes parallels from north to south. The number of available data points decreases moving from the equator to the poles.

2.2 Methods

2.2.1 Sea Ice Area Trends

Changes in sea ice area were calculated using the NSIDC sea ice concentration data set. Here it is necessary to make a distinction between sea ice "area" and sea ice "extent." Due to the error associated with surface melt and uncertainties in the marginal ice zone, a threshold filter of 15% concentration or higher is applied to define the sea ice "extent" area. The sea ice "extent" thus includes the entire area covered by above 15% concentration. This derived sea ice extent was not used in this study. Changes in ice concentration at the interior of the ice edge were of interest, and as the study progressed it was evident that winter time trends were of greater importance and wintertime data are less susceptible to errors associated with surface melt. Sea ice "area" is defined by summing the product of each grid cell area with its ice concentration as a function of time on both monthly and daily scales. 1000 km^2 was selected as a base unit.

$$A_{ice}(t) = \sum_{i=1}^{m} \sum_{j=1}^{n} C(x, y, t)_{ij} \, A(x, y)_{ij} \qquad (1)$$

Here A_{ice} is sea ice area, C is concentration of each grid cell as a function of time, and A is the area of each grid cell that changes based on the unique distortion of each cell in the polar stereographic projection as shown in Figure 7.b.

Sea ice area was computed for the north and south boxes of the study area, as well as for the sum of the two. This calculation was further refined into seasonal maxima and minima based on the annual cycle of sea ice advance and retreat. A common approach to isolating the annual maximum or minimum is to simplify by examining the maximum sea ice area in March and September respectively. In this region I found this to be an oversimplification based on the almost even distribution of annual maxima and minima between different neighboring months. For this reason, the annual max/min was computed as an average between the two months with the most frequent extrema. For the winter months, March and April were used to compute the average maximum in the north box while April and May were used to compute the average maximum in the south box. August and September were used to compute the average minimum for both boxes.

2.2.2 Sea Ice Area Transport

Sea ice surface area transport (1000 km^2 /month) was calculated by using the Fram Strait (79°N) between Greenland and Svalbard, and the Denmark Strait (Kögur Section) between Greenland and Iceland as gates for the flow of sea ice into and out of the study area. The 1000 km^2 /month unit was selected to best conform with previous studies. Required data sets were monthly NSIDC sea ice concentration and monthly NSIDC Polar Pathfinder sea ice motion

vectors. The Polar Pathfinder data set relies on the same NASA Team algorithm utilized by the sea ice concentration data set. Two methods for computing area transport were employed.

The first method relied solely on sea ice motion vectors. The Polar Pathfinder data set applies a 15% threshold concentration filter to each 25 x 25 km grid cell to round to either 100% or 0%. This can thus be viewed as transport of sea ice "extent". The result is that every cell with a vector assigned is therefore understood to contain full ice coverage. Computing the overall horizontal extent of the ice-covered cells (ΔX_{extent}), taking the cross-strait mean of velocity components ($\bar{v}$), and integrating on a monthly time scale (T) results in monthly area export values with units of square kilometers per month.

$$A_{Export}(t) = \bar{v}(t)_{Strait} \cdot \Delta X(t)_{Extent} \cdot T \qquad (2)$$

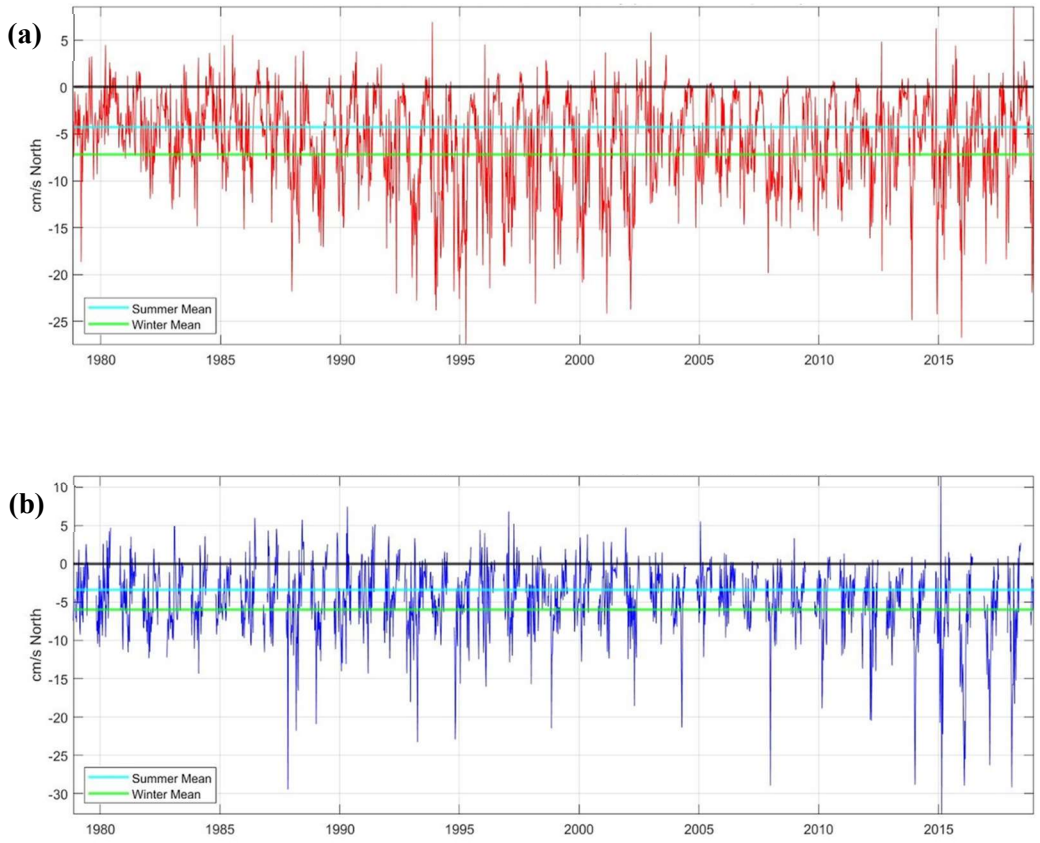

Figure 9. *Mean velocity across (a) the Fram Strait (southward component) and (b) the Denmark Strait (perpendicular component). Values are plotted weekly in units of cm/s north.*

Cross-strait velocity averages were computed using only the component perpendicular to the Fram Strait and Denmark Strait Gates. This was the purely southward component (v) for the Fram Strait, and the component perpendicular to 332° T for the Denmark Strait. Figure 9 depicts these components with weekly values in centimeters per second north, and Figure 10 depicts the geometry of sea ice motion vector components in the Denmark Strait. Weekly values in their original form are plotted in figure 9, however for the purpose of this study weekly values were averaged into monthly velocities.

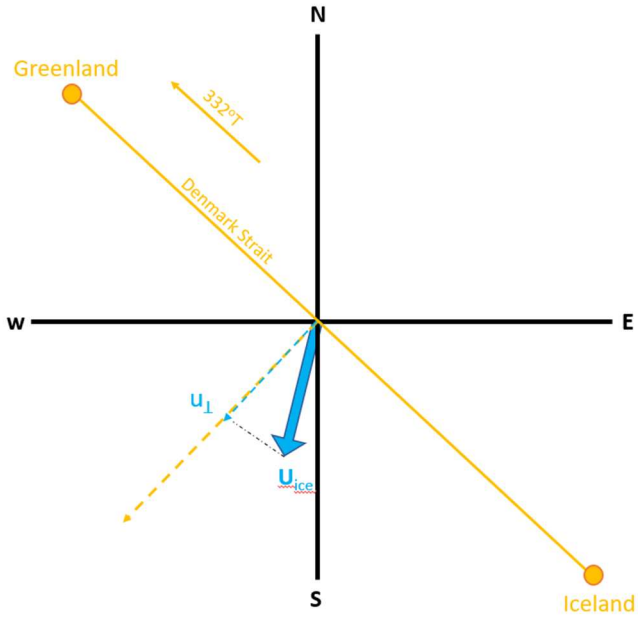

Figure 10. *Geometry of sea ice motion across the Denmark Strait.*

Isolating velocity components first required applying a rotation matrix to the velocity components (u,v) that are provided in the data set as along the EASE grid. Equations (3) and (4) were used for the transformation from the EASE domain (u is positive to the right, v is positive up) to a geographic domain (u is positive to the north, v is positive to the east). λ is longitude. Resultant magnitudes (U) were not used.

$$u_{East,West} = u_{left,right} * cos\ (\lambda) + v_{up,down} * sin\ (\lambda) \qquad (3)$$

$$v_{North,South} = -u_{left,right} * sin(\lambda) + v_{up,down} * cos(\lambda) \qquad (4)$$

The second method resembled the first in that provided velocities were transformed to a north/south domain, and only perpendicular components were used. In this case however, sea ice concentration of each cell was retained and cross-strait velocity components were not averaged. This required linear interpolation of velocity (v) and concentration (C) data to the same points evenly-spaced at 25 km intervals (ΔX) across each strait (equation 5). 24 points were used for Fram Strait and 11 points were used for Denmark Strait (Table 1). This was calculated for a monthly time scale in seconds (T). This is the more accurate transport of sea ice area.

$$A_{Expor}(t) = v_i(t) \cdot C_i(t) \cdot \Delta X \cdot T \qquad (5)$$

Table 1. *Geographic locations of points spaced at 25km across the Fram and Denmark Straits*

Denmark Strait	Lat (°N)	68.64	68.44	68.25	68.06	67.86	67.67	67.47
	Lon(°E)	-25.98	-25.68	-25.39	-25.10	-24.81	-24.53	-24.26
	Lat (°N)	67.27	67.08	66.88	66.68	--	--	--
	Lon(°E)	-23.99	-23.72	-23.46	-23.20	--	--	--
Fram Strait	Lat (°N)	79	79	79	79	79	79	79
	Lon(°E)	-17.00	-15.82	-14.65	-13.47	-12.29	-11.12	-9.94
	Lat (°N)	79	79	79	79	79	79	79
	Lon(°E)	-8.76	-7.58	-6.41	-5.23	-4.05	-2.88	-1.70
	Lat (°N)	79	79	79	79	79	79	79
	Lon(°E)	-0.52	0.65	1.83	3.01	4.19	5.36	6.54
	Lat (°N)	79	79	79	--	--	--	--
	Lon(°E)	7.72	8.89	10.07	--	--	--	--

2.2.3 Thickness

Using the PIOMAS model sea ice thickness output, monthly values for the length of the study period were plotted and transformed to the NSIDC polar stereographic grid. For thickness estimates across the Fram and Denmark Straits, manual selection was used to identify cross-strait indices. Since the grid is natively aligned north and south, cell selection across 79° N (Fram Strait) resulted in a continuous line of consecutive grid cells. For Denmark Strait, the selected line section did not align with the grid, so two stripes of staggered cells were selected and averaged to create a continuous section without gaps.

2.2.4 Volume Transport

Volume transport calculations resembled the area transport calculations closely, with the addition of a thickness variable *H.* Again, two methods were employed (equations 6 and 7):

$$V_{Export}(t) = \bar{v}_{Strait}(t) \cdot \bar{H}_{Strait}(t) \cdot \Delta X_{Exten}\ (t)\ \cdot T \qquad (6)$$

$$V_{Export}(t) = v_i(t)\ \cdot\ C_i(t) \cdot \Delta X \cdot H_i(t) \cdot T \qquad (7)$$

Method one (equation 6) uses strait-averaged values for thickness and velocity, and the width of the sea ice extent (ΔX_{extent}) parallel to each respective strait. Method two (equation 7) uses linear interpolation of grid values to different points (subscript indices *i*) evenly spaced (ΔX) across the straits. In both cases again only the perpendicular component of the velocity was used, and *T* denotes a monthly period in seconds.

Where 25 km was the constant ΔX for the area transport calculations, incorporating the PIOMAS data set for thickness introduced a finer-resolution data set. The 1° resolution of the

PIOMAS grid means that the distance between grid points in the zonal direction is a function of latitude. At 79°N, grid points spaced at every degree of longitude are 21.22 km apart, so a revised ΔX of 21 km was applied for use in the volume transport calculations. This increased the number of points from 24 to 28 in the Fram Strait, and from 11 to 13 in the Denmark Strait. Updated points are included in Table 2.

Table 2. *Geographic locations of points spaced at 21km across the Fram and Denmark Straits*

Denmark Strait	Lat (°N)	68.64	68.48	68.31	68.15	67.99	67.82	67.66
	Lon(°E)	-25.98	-25.73	-25.48	-25.24	-24.99	-24.75	-24.52
	Lat (°N)	67.49	67.33	67.16	67.00	66.83	66.67	
	Lon(°E)	-24.29	-24.06	-23.84	-23.62	-23.40	-23.18	
Fram Strait	Lat (°N)	79	79	79	79	79	79	79
	Lon(°E)	-17	-16	-15	-14	-13	-12	-11
	Lat (°N)	79	79	79	79	79	79	79
	Lon(°E)	-10	-9	-8	-7	-6	-5	-4
	Lat (°N)	79	79	79	79	79	79	79
	Lon(°E)	-3	-2	-1	0	1	2	3
	Lat (°N)	79	79	79	79	79	79	79
	Lon(°E)	4	5	6	7	8	9	10

2.2.5 Volume Budget

A winter time volume budget for the north box was derived in order to compare the relative magnitudes of sea ice imported and exported, and forming/melting locally. For each

month for the length of the record, including summer months, the monthly sea ice area value calculated in 2.2.1 was combined with a monthly representative thickness from PIOMAS. The representative thickness was defined as the mean PIOMAS thickness of all grid cells in the north box ignoring values less than 1 cm. Equation 8 describes this method. The subscripts *i* and *j* represent cell x/y indices, *V* is the calculated volume, A_{ice} is sea ice area, and $\overline{H}$ is mean thickness.

$$V(t) = A_{ice}(t) \cdot \overline{H}_{ij}(t) \quad (8)$$

Years were averaged into two mean annual cycles: one cycle representing the timeframe during which a feature called the Odden Ice Tongue was reliably present (discussed in greater detail in section 3.1.2), and one cycle for the time period when it no longer appeared. The local minimum was subtracted from the local maximum in each cycle to obtain winter volume change values.

$$\Delta V = \left(A_{ice} \cdot \overline{H}_{ij}\right)_{max} - \left(A_{ice} \cdot \overline{H}_{ij}\right)_{min} \quad (9)$$

Those values were compared with volume flux and convergence values to derive a local change (positive for freezing, negative for melting).

$$\Delta V_{local}(t) = V_{Import}(t) - V_{Export}(t) - V(t) \quad (10)$$

2.2.6 Heat fluxes

Scalar fields were examined for sea surface temperature (°C), latent heat flux (W/m^2), incoming shortwave radiation (W/m^2), outgoing longwave radiation (W/m^2), and sensible heat flux (W/m^2). Using known pathways of warmer Atlantic water (figure 5), a box of interest was

selected west of Norway to examine any changes in these parameters over the course of the study period. Values were averaged over the area of the box for each month.

CHAPTER 3: RESULTS

3.1 Sea Ice Area

3.1.1 Study Area Trends

Time series of sea ice area in each of the north and south boxes over the length of the record using monthly data show significant temporal variability (Figure 11). Sea ice area in the southern box is only about one fourth the size of the ice area in the north. Being farther south there is little local formation, and most of the sea ice present in the area over the course of the winter is advected into the box from the north in the Greenland Coastal Current.

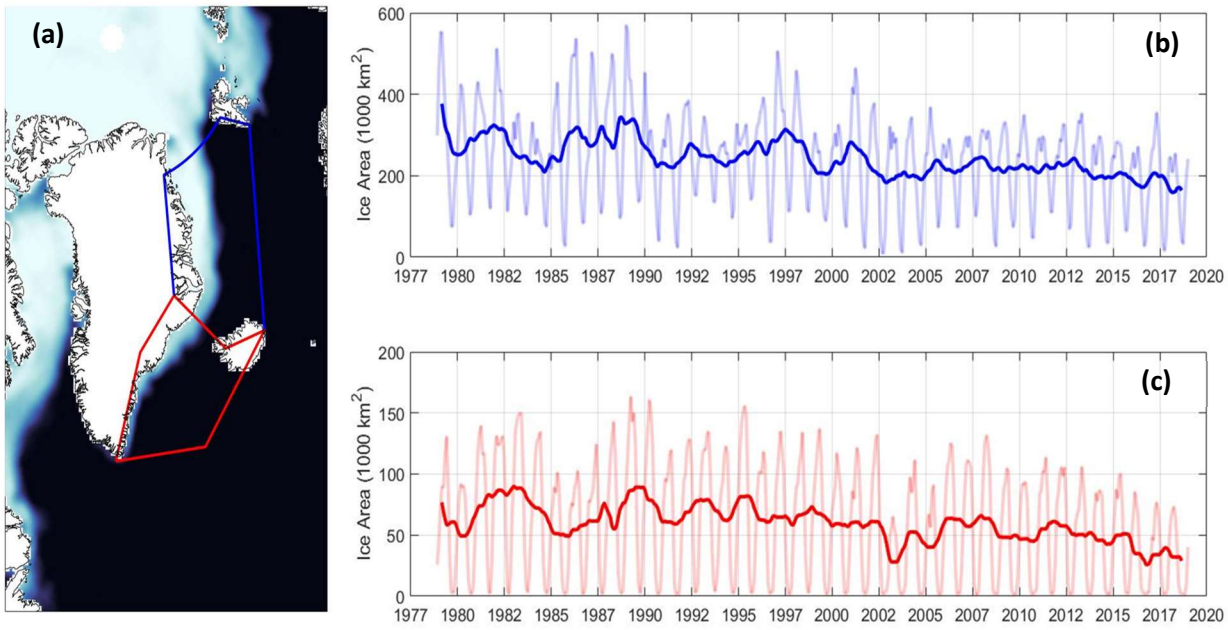

Figure 11. *(a) Limits of north and south boxes in the study area. (b) Time series of monthly sea ice area in the north box in 1000 km^2. (c) Time series of monthly sea ice area in the south box in 1000 km^2. Thick solid lines depict 12 month moving averages. The scale of the vertical axes changes between (b) and (c).*

Like most of the Arctic, the north and south study areas are seeing a decrease in sea ice coverage during both the summer and the winter. Figure 12 depicts the decrease in sea ice area

using the average of two months to represent the annual maximum or minimum. For the winter maximum sea ice area, March and April values were averaged for each annual value in the north box, and April and May values were averaged in the south box. For the summer minimum sea ice area, August and September values were averaged for both boxes. Figure 12.c depicts the timing of the maximum and minimum by month for the length of the study.

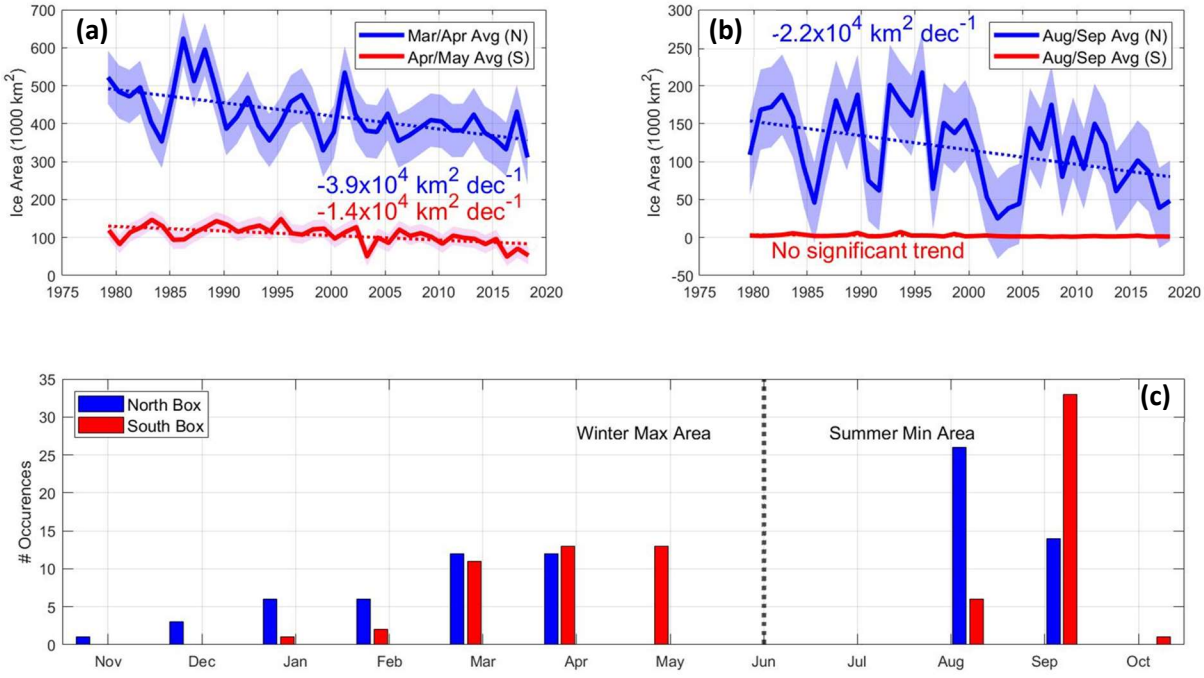

Figure 12. *(a) Trend in winter maximum sea ice area for north (blue) and south (red) boxes. Shaded regions are series standard deviations. (b) Trend in summer minimum sea ice area for north and south boxes. Axes scale changes from (a). (c) Timing of annual maxima/minima by*

The winter maximum in the northern box is experiencing the greatest sea ice loss from year to year out of each of the four scenarios (north/south box, summer min/winter max). Onarheim et al. (2018) also found the decrease in the winter maximum to be the prevailing trend in the area. Over the length of the record in the north box, linear fits to 95% significance indicate that sea ice area decreased by 11.6% (-39,000 km^2 per decade) during the winter and 6.7% in the summer in reference to the size of the box (-22,000 km^2 per decade). In the south box, the winter

trend is -6.4% over the length of the record (-14,000 km^2 per decade., and since that area is largely ice-free in the summer there is no trend for summer minimum.

3.1.2 Loss of the Odden Ice Tongue

Next, it was necessary to examine to what extent the negative trend in sea ice coverage in the northern box can be attributed to progressive disappearance of a sea ice feature characterized

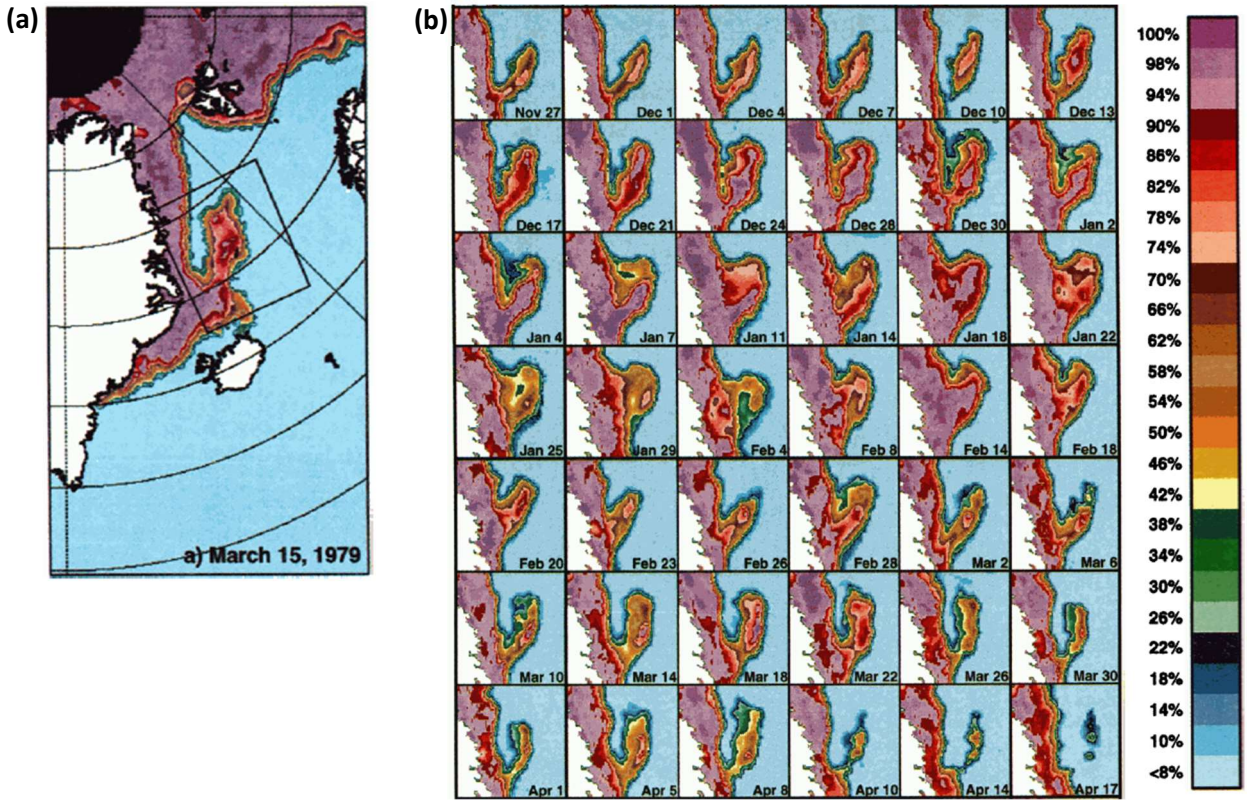

Figure 13 (Comiso et al. 2001). *(a) Area of Odden development in Greenland Sea (black box). (b) Example of Odden development from the 1996-97 season.*

by local sea ice formation called the Odden Ice Tongue. As described by Comiso et al. in 2001, the Odden Ice Tongue is "an ice cover phenomenon in the Greenland Sea that covers all or part of the area of influence of the Jan Mayen Current and that encloses a bay of open water called "Nordbukta." A depiction of a typical Odden year from Comiso et al. (2001) illustrates how it

develops progressively over the course of a winter (Figure 13). The Odden Ice Tongue is the portion of sea ice that protrudes into the center of the Greenland Sea. Deser et al. (2000) also attribute the variability of sea ice in the Greenland Sea to the Odden Ice Tongue.

In-depth characterizations of the Odden were presented in Wadhams and Comiso (1999) and Comiso et al. (2001). The ice tongue ranges in size from 250,000 – 330,000 km^2 and grows outward from the ice edge into the Greenland Sea. Although evidence is presented in Wadhams and Comiso (1999) that it is sometimes formed by older sea ice advected offshore, it typically forms locally as frazil-pancake ice. Wilkinson (2006) found similar ice types in the Odden. Wave activity in the area is high, which prevents a continuous sheet of sea ice from forming. Since the water's surface isn't completely blanketed by sea ice, it allows for increased ocean-atmosphere heat flux and subsequent increased sea ice growth rates. Limited observations of sea ice in the area suggest typical pancake thickness of 20-30 cm (Shuchman et al. 1998) and typical ice floe thickness (advected from the East Greenland Current) of 1-2 meters (Wadhams and Comiso 1999). The Odden Ice Tongue was a relatively well-documented phenomenon while it was reliably present, however since 2004 there has been little focus on the feature since it no longer exists. Here I use the timing of its disappearance as a reference point between two distinct regimes of mean sea ice concentration and volume.

Figure 14.d shows a time series of all winter months (November – April) for the duration of the study period. Instances of the Odden appearing are marked in magenta. In order for a year to be declared an Odden year, the sea ice concentration in the area depicted in figure 14.a had to have experienced at least one month with an average of 1% sea ice concentration or more. The blue series in figure 14.d represents changes in winter sea ice area over the entire study area, while the red series represents changes in sea ice area over the continental shelf, defined here as

the area shoreward of the 500m isobath (see Figure 14.d). The difference in the blue and red series is attributed to the Odden, last appearing in 2004. As the Odden disappears over time, the two series converge to a much higher degree of correlation after 2004 (R=0.63 before vs. R=0.89 after). This supports the finding that the Odden was driving most of the variability in the entire study area before it disappeared. Linear fits to 95% significance show a decadal loss of 3.4% for the entire area that includes the Odden, and a 0.21% decadal loss for the shelf region that excludes it. Following analyses were conducted with the 2004 season identified as a transition point between a so-called "Odden era" and "Odden-free era."

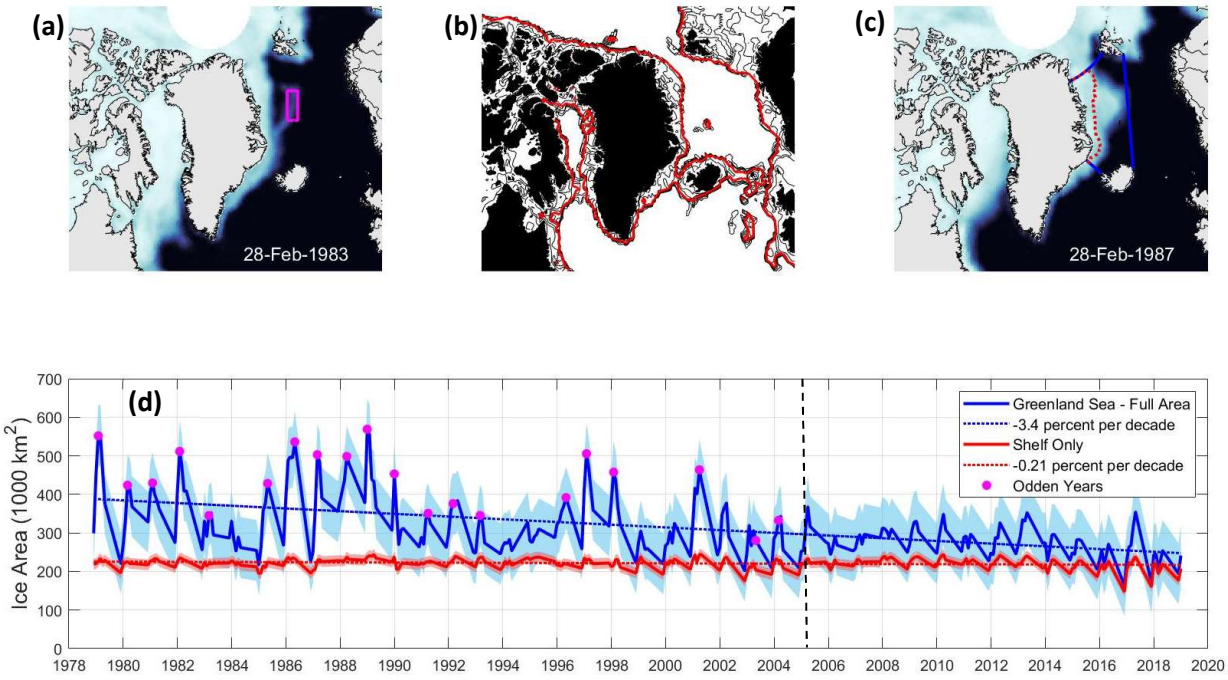

Figure 14. *(a) Boundaries of Odden "detection" area. Average monthly sea ice concentration of 1% or greater resulted in the designation of an Odden year. (b) ERA5 Bathymetry with 500m isobath highlighted in red. (c) The north box outlined in blue and the 500m isobath outlined in red. (d) Corresponding winter time series (November through April) for the north box (blue) and the shelf box (red). The black dotted line is the demarcation line between the "Odden" and "post-Odden" eras as defined in this study. Magenta dots indicate Odden year. Shaded regions indicate one standard deviation.*

3.1.3 Effect of the Odden Ice Tongue on the Winter Maximum

Figure 15 depicts the annual cycle of sea ice area in the north box. Each line in the plot is the mean cycle of daily resolution data points binned into 5-year means. Each averaged cycle is smoothed with a 12-day running mean, and the local maximum and minimum are plotted once per cycle. Both the plotted maxima and minima exhibit negative trends in amplitude, with the greater decline again evident in the winter months (black arrows).

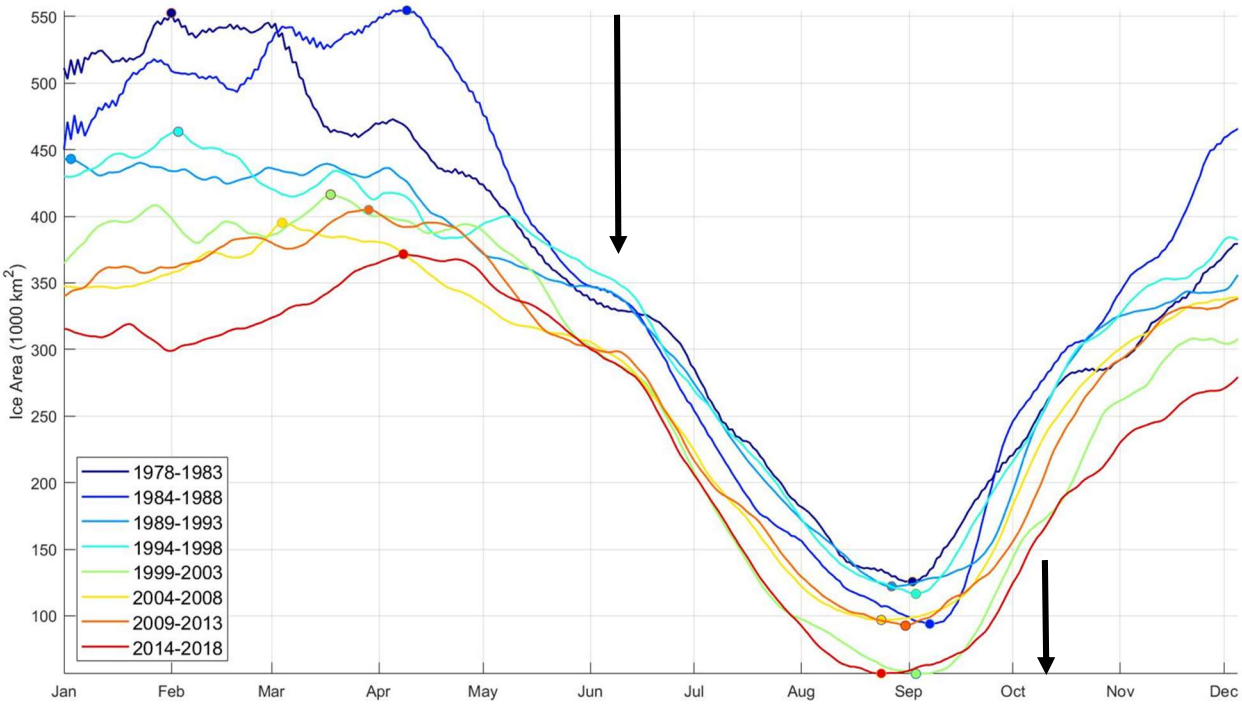

Figure 15. *Average annual cycle of sea ice area in 5-year bins plotted using a 12-day moving mean. Black arrows represent change in amplitude annual maximum/minimum.*

The wintertime maxima are much more clearly pronounced for the three most recent cycles (yellow, orange, and red). At the beginning of the record the winter time maximum was less pronounced; it was more a broad plateau that was typically reached in February and persisted until March or April. After the disappearance of the Odden, the inflection points between growing and melting sea ice are much more easily identified and the annual cycle resembles more a sinusoid with Maxima in March and April. Prior to 2004, the local sea ice

formation at the surface and its variable timing (the Odden did not consistently occur in any one month) acted to obscure the more consistent advection-driven seasonal max in late March or early April that otherwise does exist but was more challenging to identify because of the Odden. In the current Odden-free era, advected sea ice builds up to a seasonal maximum without the concealing effect of the Odden.

3.1.4 Sea Ice Area Transport

Figure 16 depicts estimated sea ice area transport across Fram Strait and Denmark Strait (see Chapter 2.2 for method). The blue lines incorporate variable sea ice concentration across the

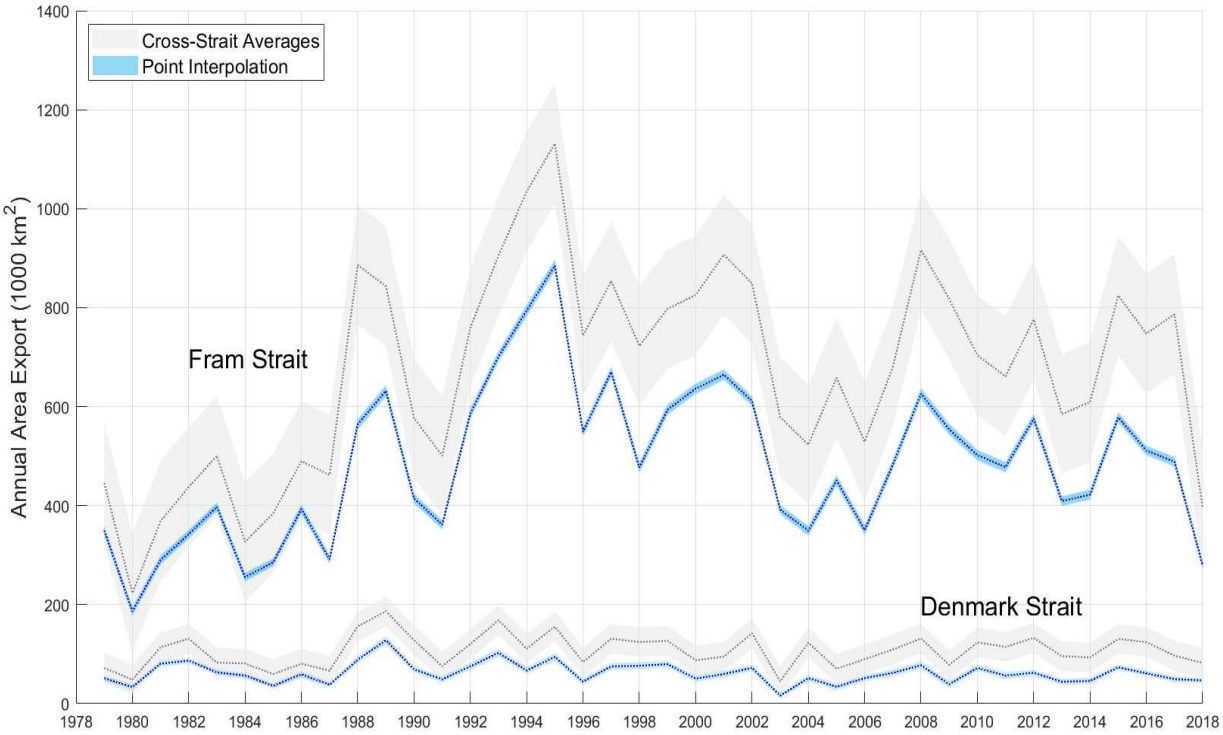

Figure 16. *Annual sea ice area export across Fram Strait at 79°N and Denmark Strait along the Kögur Section in 1,000 km^2. The blue lines are the result of interpolating concentration and velocity to evenly spaced points. The gray lines depict the average velocity of sea ice extent along 79°N (grid cells wheresea ice concentration is greater than 15% is assumed to be 100% concentration). Shaded areas represent the product of uncertainties associated with each data set.*

straits into the equation and linear interpolation of concentration and velocity to the same evenly-spaced points. The curves shown in gray are obtained by assuming 100% concentration for every grid cell that was assigned a motion vector, and averages velocity values across the strait. The quite similar temporal evolution illustrates that the sea ice concentration is close to 100% and the velocity is quite homogeneous across Fram Strait. Intuitively the gray lines are consistently higher than the blue lines in each case because of the 100% sea ice concentration assumption. The two methods are shown only for comparison since the blue lines are the more accurate approximation of the area transport across each strait. Values are annual sums plotted once per year.

A linear fit to the sea ice area export (blue line) for Fram Strait suggests a slightly positive trend over the course of the record but is not significant at the 95% level ($p=0.13$). A similar fit to the averaging series for Fram Strait (gray line) is significantly positive, but again this series is inherently less reliable because concentration is not incorporated. Therefore this analysis indicates that sea ice area transport across Fram Strait is largely unchanged between 1979 and 2018. The Denmark Strait transport shows no significant trend and typical values are an order of magnitude smaller than respective Fram Strait values.

3.2 Sea Ice Thickness

The PIOMAS sea ice output was used to examine trends in sea ice thickness, especially across the Fram Strait and the Denmark Strait in order to examine changes in volume transport across those selected gates. A Hovmöller diagram showing a time series of changes in cross-strait thickness for each one of the straits (Figure 17) shows a strong annual cycle is apparent in

both sections, with thicker sea ice present in the winter months. The Denmark Strait is typically ice-free during the summers, and has a wintertime thickness of less than 1m. In the Fram Strait, the thickest ice is found towards the center of the strait where multi-year sea ice flowing south from the Arctic isn't impeded by the land-fast sea ice to the west. The thicker ice ranges between 2 and 5 meters in draft. Drafts of 3 meters or greater are common throughout the record up to May 2004, after which there are no drafts greater than 3 meters.

The 2004 season previously identified as a demarcation point between two distinct eras of sea ice concentration is similarly a demarcation for sea ice thickness across the Fram Strait. If one were to draw a horizontal line across figure 17.a at 2004, the mean states above and below the line are very different.

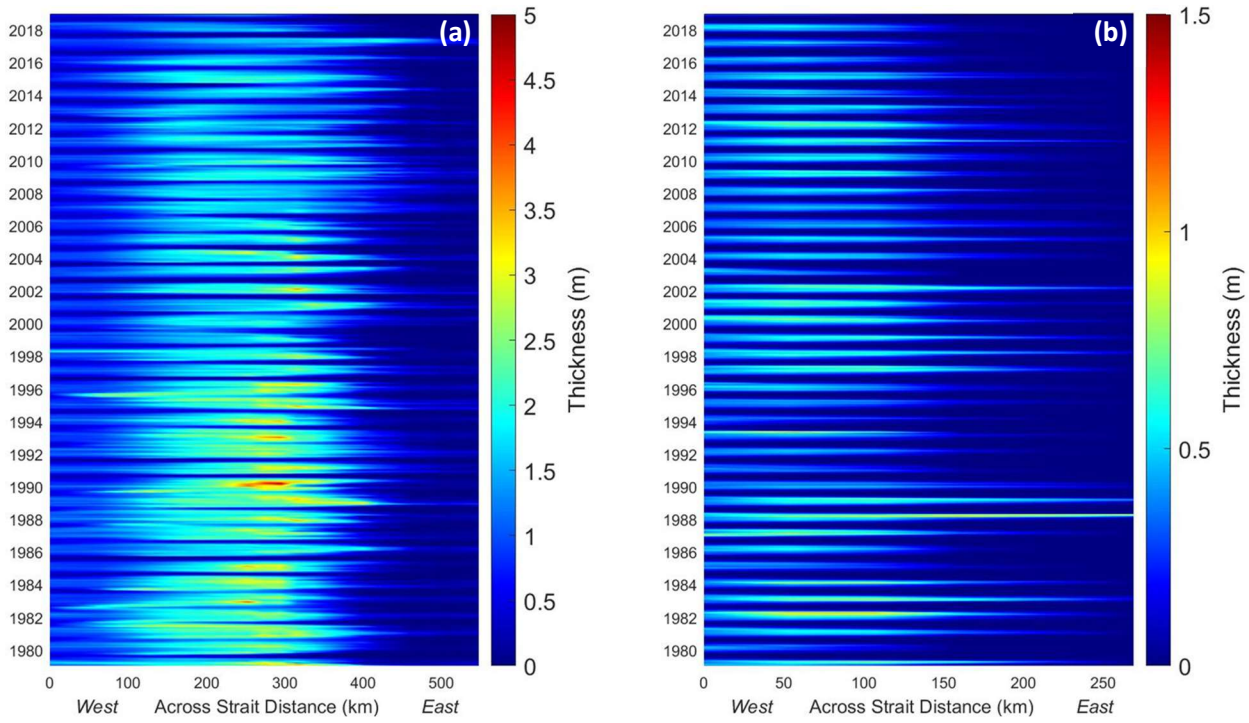

Figure (17). *PIOMAS ice thickness across (a) Fram Strait and (b) Denmark Strait. Colorbar and horizontal axes scales change between the two images.*

Figure 18 represents this change by depicting the mean annual cycle of sea ice thickness across Fram Strait before and after 2004. The mean thickness across the strait in March in the

1979-2004 period was 1.3 meters, and for 2005-2018 it was 1.08 meters, which is a 15.3% reduction in winter maximum sea ice thickness across Fram Strait. This has significant implications for the volume of sea ice flowing south from the Arctic.

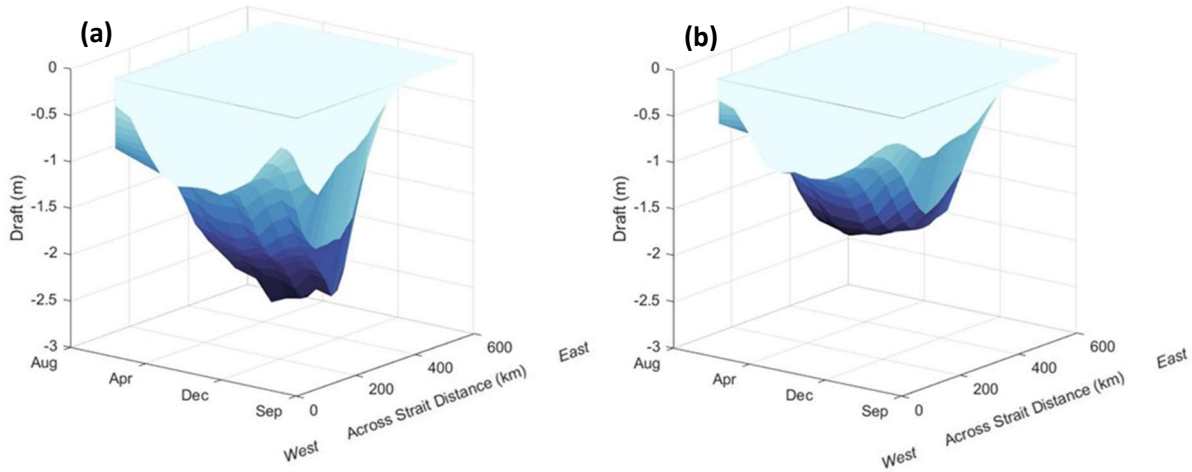

Figure 18. *Mean annual cycle of sea ice draft (thickness) across Fram Strait for (a) 1979-2004 and (b) 2005-2018. The x-axis is distance along 79°N latitude, the y-axis is one annual cycle from September-August (from right to left), and the z-axis is draft beneath the surface.*

3.3 Volume Transport

Figure 19 depicts the results of the volume transport calculations described in Chapter 2.2.4. The mean annual cycle for the whole record is given as the bold line, with the annual maximum plotted with a single black point. Individual years are plotted on the same axis and colored by time.

Volume Transport across Denmark Strait is an order of magnitude smaller than across Fram Strait. Typical values for sea ice transport across Fram Strait during winter months are on the order of 100 km^3/month while only about 5 km^3/month make it down the east coast of Greenland to cross the Denmark Strait. The dominant effect that the East Greenland Current has on the advection of sea ice down the coast is evident in the two-month lag between when sea ice

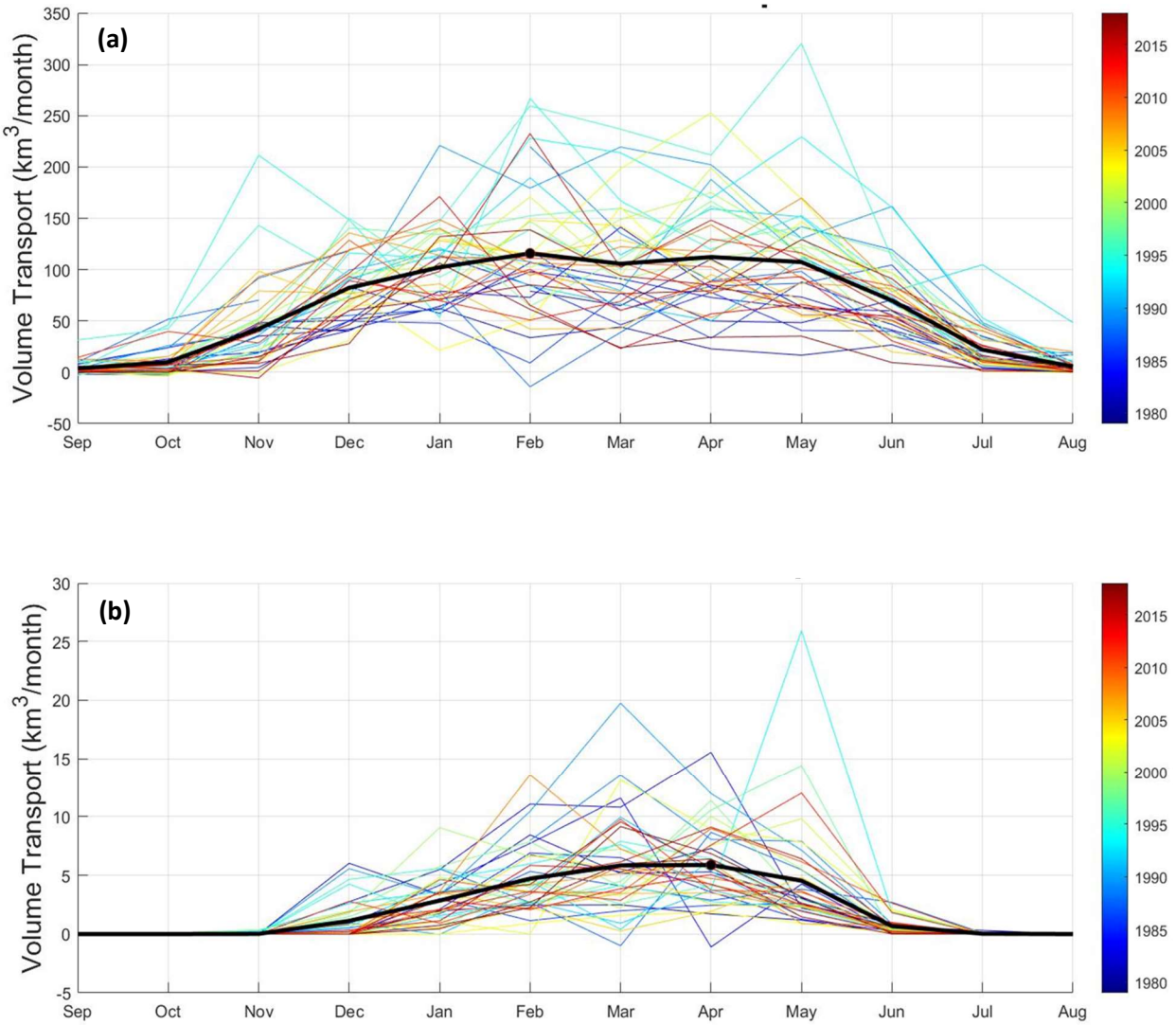

Figure 19. *(a) Volume transport in km^3/month across Fram Strait. Mean annual cycle with winter maximum plotted in black. (a) Volume transport in km^3/month across Denmark Strait.*

begins to flow across 79°N (September) and when it starts to flow across Denmark Strait (November). Similarly, the seasonal retreat of sea ice up the coast can be seen in the time between when transport goes to zero for the Denmark Strait (typically July) and when it reaches the minimum in Fram Strait (August).

For the Fram Strait, years earlier in the record (up until the mid-90s) experienced below average volume transport. During the mid-90s to the early 2000s the transport was well above average, and during the most recent third of the record it was consistently below average.

Applying the same pre/post 2004 separation utilized in prior analyses shows a systemic decrease in seasonal volume export between the two periods. Integrating winter export from September to March across Fram Strait gives a cumulative, mean value of 475 km^3 through 2004, and 421 km^3 in the period afterwards (11% decrease). Integrated values for these winter months at the Denmark Strait are again on an order of magnitude smaller, and largely unchanged (16 km^3 on average before 2004 and 12 km^3 after 2004). Figure 20 is a time series of seasonal volume export from September through March at each gate. Values are plotted once annually. Denmark Strait values are difficult to interpret at this scale but are included as a reference for the magnitude of the difference between the export at each gate.

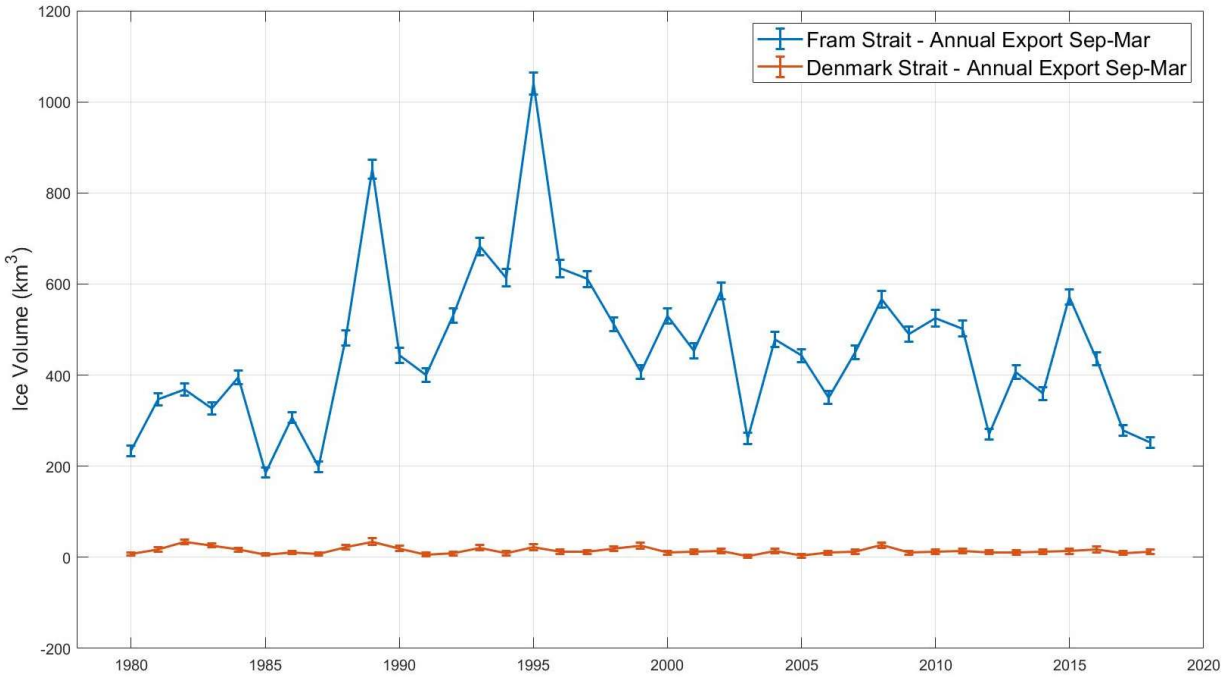

Figure 20. *Seasonally integrated volume transport for Denmark Strait and Fram Strait from September through March. Error bars represent the multiplication of uncertainties for thickness, concentration, and velocity at each interpolation point summed for each Sep-Mar season.*

3.4 Volume Budget

3.4.1 Seasonal Change

My estimates of volume transport across the two gates are next used to construct a sea ice volume budget for winter in the northern study area. Here I define sea ice convergence as the difference between sea ice entering the box at 79°N and sea ice leaving the box at Denmark Strait. "Convergence" instead of "divergence" is used in this case because sea ice accumulates in the box due to the overwhelming volume of sea ice flowing in compared to the almost negligible amount of sea ice flowing out (~450 km^3 per winter versus ~15 km^3 per winter). With no sea ice exiting out the eastern boundary between Iceland and Svalbard, even during Odden years, the system is closed with the exception of local ice formation and melt. To examine the relationship between sea ice flowing into the north box and the local change in volume, monthly volume estimates were calculated using remote-sensing derived sea ice area values from the north box

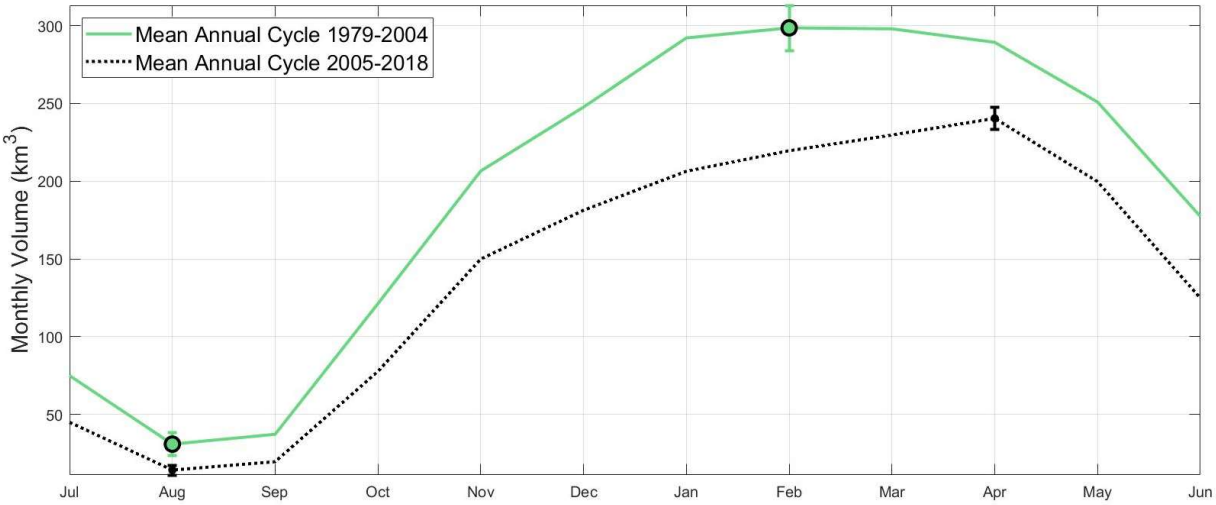

Figure 21. *Annual cycle of sea ice volume in the north box up through 2004 (green) and after (black). Green and black points are placed at local maxima and minima. Error bars show the standard error of the averaged quantities.*

and thickness from PIOMAS from the same month. Mean annual cycles were calculated for the "Odden" and "Post-Odden" eras and are presented in figure 21.

The analysis presented in Figure 21 supports two results. The first is the shift in the timing of the winter maximum in sea ice volume. As discussed in Chapter 3.1.3, the Odden Ice Tongue broadened the winter maximum that includes the advection-driven maximum. In examining the winter months of the green series (1979-2004), the monthly sea ice volume is almost constant between January and April. The maximum value is in February, but the plateau-like feature of the cycle is apparent and creates more of a broader, more persistent maximum from January to April. Any of those months are within the standard error. In the more recent record, the maximum is clearly in April, and is a distinct inflection point between sea ice convergence and melting now that there is no Odden and relatively little sea ice formation.

Figure 21 also depicts the shift in amplitude of the maximum and minimum sea ice volume. For the Odden Era, the summer minimum was 31 km^3 and the winter maximum was 299 km^3. For the contemporary time period, 14 km^3 is the mean summer minimum and it grows to 240 km^3. The post-Odden winter growth season begins with roughly half the sea ice volume and grows 42 km^3 less than winters before 2004.

3.4.2 Odden Ice Tongue Contribution

The Odden Ice Tongue contributed to the seasonal change in sea ice volume while it was still reliably present. Shuchman et al. (1998) found from on-site observations that typical ice pancake thickness within the Odden was between 20-30 cm. The mean PIOMAS thickness in the same Odden "detection area" (see Figure 14.a) used to identify years the tongue formed is 27 cm. Using the 20 and 30 cm as lower/upper bounds combined with the mean sea ice area of the 20 identified Oddens (209,460 km^2) indicates that the additional ice volume due to the Odden is

between 42 and 63 km^3 each winter. The sea ice area of the each Odden was determined by taking the sea ice area of all ice seaward of the 500m isobath during the month of the seasonal maximum. This was only done for years that met the Odden criteria. Figure 22 depicts the volume of each of the 20 Odden Ice Tongues (indicated in figure 14) using PIOMAS thickness in the detection area and sea ice area seaward of the 500m isobath. Treating the 1979 Odden as an extreme outlier and excluding it, the mean contribution of the Odden to sea ice volume is 53 km^3.

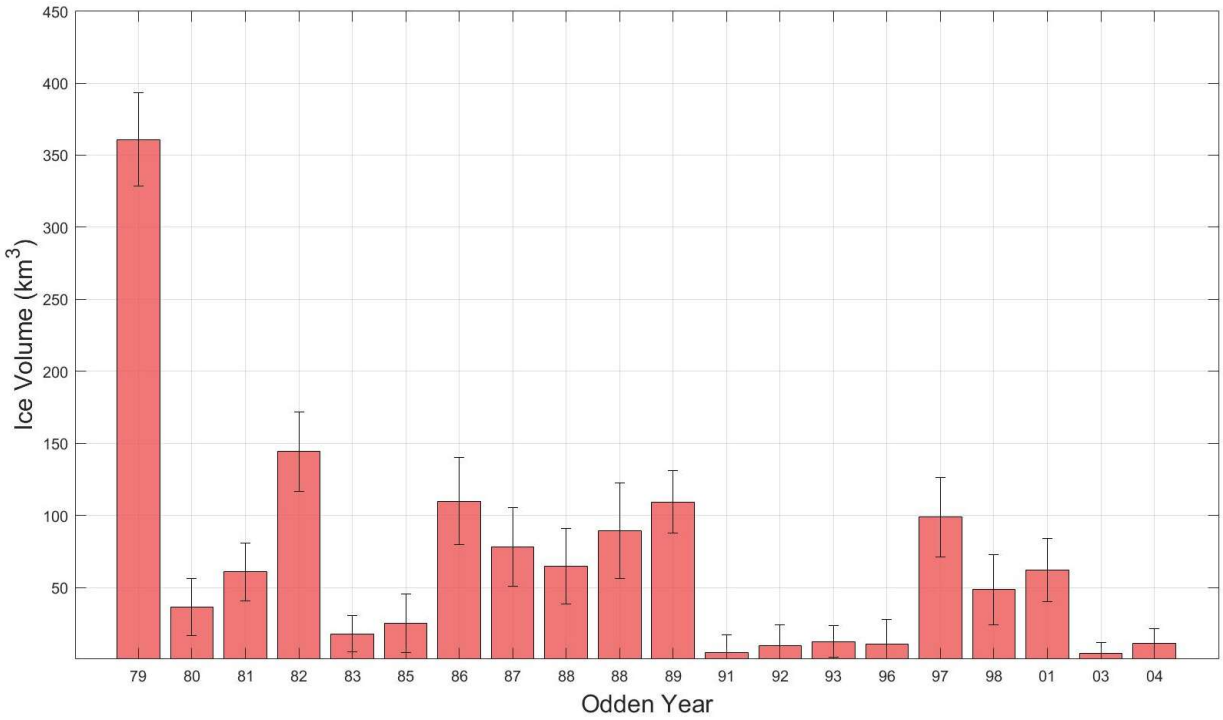

Figure 22. *Volume of each Odden Ice Tongue over the course of the record using PIOMAS thickness and sea ice area seaward of 500m isobath. Error bars indicate the root square sum of uncertainties from each data set.*

From the variability in the month-to-month volume change and the sea ice transport in and out of the box, I estimate the wintertime budget for the northern box. Mean seasonal sea ice convergence values (where "convergence" is equal to the volume of sea ice in minus the volume

of sea ice out) are much higher than the seasonal change in volume, implying a high degree of melting, even during winter time. Up until 2004, the mean sea ice volume convergence in the area from September to March was 459 km^3. This value does not include the 1979 season since it was incomplete (beginning in January). From 2005 onwards the mean convergence was 409 km^3. Compared to the mean volume change estimates from figure 21, about half of the sea ice that flows into the area must melt over the course of the winter. Table 3 summarizes volume budget values for the Odden and Post-Odden Eras.

Table 3. *Winter volume budget for the north box of the study area with standard errors of the averaged years and summed where appropriate (lines 5 and 6).*

		1979-2004	**2005-2018**
(1) ΔVolume in North Box (min to max)		268 ± 22	226 ± 10
(2) Odden Contribution to (1)		53 ± 18	0
(3) Fram Strait Winter Import (Sep to Mar)		475 ± 38	421 ± 31
(4) Denmark Strait Winter Export (Sep to Mar)		16 ± 2	12 ± 1
(5) Volume Convergence	(3) – (4)	459 ± 38	409 ± 31
(6) Local Freezing (+) or Melting (-) in North Box	(5) – (1)	-191 ± 44	-183 ± 33
(7) Melt fraction of advected sea ice	(6) / (5)	41%	44%

CHAPTER 4: DISCUSSION

4.1 Errors and Uncertainties

Each of the data sets used in this study is subject to different sources of error. The first data set, NSIDC sea ice concentration, is subject to uncertainties of several varieties as outlined in Cavalieri et al. (1984). Passive microwave sensors are unable to unambiguously distinguish between multiyear ice (MYI) and first-year ice (FYI); accuracy decreases as the proportion of thin FYI increases. The microwave signature of snow on top of sea ice acts to obscure the true concentration by up to 8% and surface winds roughen the ocean surface which depolarizes received radiation. Errors associated with atmospheric opacity and heavy cloud cover, although generally small, affect the received radiation differently over open ocean and over ice. Furthermore, the selected polarization of the instrument (vertical vs. horizontal) experiences significant differences in variability. Finally, melt ponds on top of sea ice, particularly in the summer months, affect the accuracy of total sea ice concentration. In general, as a result of these uncertainties the total sea ice cover is within 5% of the actual sea ice concentration in winter/spring, and within 15% in the summer/fall (NSIDC). The 15% threshold for converting “sea ice area” to “sea ice extent” is based off of this uncertainty.

Uncertainty in the Polar Pathfinder data set is provided in the form of weighted cross correlations of input sources (described in Chapter 2) with motion vectors from the International Arctic Buoy Program. Error variance values are assigned to each daily vector, and for the weekly vectors each value is accompanied by the number of observations (N) that contributed to the data point. Since only daily values had the assigned error value and since weekly vectors were then averaged into monthly values for the purpose of this study, the individual daily variance values were not utilized. A broader estimate of the accuracy of the product was examined based on the derivation of sea ice motion process described by the NSIDC. Each of the input sources (passive microwave,

radiometer, and surface winds) were evaluated against the motion of buoys within 50 km, and the mean difference and root mean square (RMS) error of each comparison with *N* observations is shown in table 4. Since the buoys flow with the sea ice, the error associated with the movement is only due to the position accuracy (within 0.5 km) and grid interpolation error. It is assumed that overall buoy error is less than 1 cm/s for the average velocity over 24 hours (NSIDC) and is the most accurate of the input sources. The least accurate is the NCEP/NCAR winds, which also have a coarse resolution of about 250 km. However, these wind vectors are the most consistent and abundant data. Due to melt in the summer months, passive microwave data is mostly unusable for determining motion, and because cloud cover often obscures visual or infrared sea ice detection with AVHRR. Gaps are filled based on the NCEP/NCAR re-analysis wind fields which are not direct observations but from an atmospheric model. The sea ice vectors derived from this wind forcing are also only estimated based on Thorndike and Colony (1982) which state that sea ice moves at a speed of approximately 1% of the wind speed, and has a turning angle of about 20 degrees from the wind direction. Table four summarizes the numerical uncertainties in the Polar Pathfinder data set.

Table 4. *Uncertainties by instrument type in the Polar Pathfinder data set.*

	u Component		v Component		
Sensor	Mean Difference (cm/s)	RMS (cm/s)	Mean Difference (cm/s)	RMS (cm/s)	N Pairs
Passive Microwave (85 GHz Channel)	-0.05	4.16	0.39	4.23	74,381
Passive Microwave (37 GHz Channel)	0.04	5.05	0.74	5.24	74,381
Advanced Very High Resolution Radiometer	-0.12	3.31	0.07	3.29	26,820
	Resultant Vector (U)		--	--	--
	Mean Difference (cm/s)	RMS (cm/s)	--	--	--
NCEP / NCAR Winds	1.2	6.1	--	--	Unknown

Schweiger et al. (2011) presented results validating PIOMAS thickness estimates against two observational data sets. The first was a sea ice climate data record of thickness observations compiled by Lindsay (2010) from Arctic submarine missions, upward looking sonar moorings, and airborne

electromagnetic measurements. The second was a set of thickness estimates retrieved from NASA's Ice, Cloud, and Land Elevation Satellite (ICESat) that employed laser altimetry to measure sea ice freeboard by comparing laser-measured distances between ice-covered and ice-free areas from 2003-2010. Freeboard measurements were converted to thickness using a variety of processing steps (Kwok et al. 2009). Uncertainty estimates derived from that study vary based off the sensor(s) that PIOMAS was compared to in each scenario, and the uncertainty estimates themselves are uncertain because of differences in spatial domains (i.e. the satellite footprint of ICESat and U.S. military-authorized data-release area for submarines). The study found that PIOMAS typically underestimates thick sea ice, and overestimates thin sea ice, and concluded that conservative error estimates bound the potential error. These conservative estimates were the largest of the calculated errors, and were derived from the comparison between PIOMAS and ICESat thickness retrievals. The mean bias was -0.1 m in the spring months, and -0.26 m in the fall months with a root mean square error of 0.78 m. Applying those biases resulted in a reduction of Arctic sea ice volume by -6.3% in the spring and -10% in the fall.

In the case of each of these datasets, the most conservative uncertainty estimate was used to approximate errors for area and volume transport. In the case of the NSIDC sea ice concentration and the PIOMAS data sets, uncertainties varied by season, which was incorporated into each error calculation. For products produced from a single data set, the standard deviation was plotted as the uncertainty. For products produced from multiplying data sets together (i.e. for getting volume transport by multiplying area by thickness and velocity), the following expressions were used with volume transport (Φ_V) and area transport (Φ_A) as examples. δ signifies the uncertainty in the quantity, U is velocity, H is thickness, and A is area (concentration).

$$\delta\Phi_V = |\Phi_V| \cdot \sqrt{\left(\frac{\delta U}{U}\right)^2 + \left(\frac{\delta H}{H}\right)^2 + \left(\frac{\delta A}{A}\right)^2} \qquad (11)$$

$$\delta\Phi_A = |\Phi_{VA}| \cdot \sqrt{\left(\frac{\delta U}{U}\right)^2 + \left(\frac{\delta C}{C}\right)^2} \qquad (12)$$

Uncertainties for values produced by addition or subtraction (i.e. volume convergence), were calculated using equation 13. *C* is convergence, and V_{in} and V_{out} are volume transports in and out of the north box.

$$\delta C = \sqrt{\delta {V_{in}}^2 + \delta {V_{out}}^2} \qquad (13)$$

Uncertainties for averaged quantities were derived using equation 14 for the standard error where σ is the standard deviation of the averaged quantities and *N* is the number of data points.

$$SE = \frac{\sigma}{\sqrt{N}} \qquad (14)$$

4.2 Comparison to Similar Results

Estimates of sea ice area and volume transport in this study are on average lower than the results of previous studies. For sea ice area transport, results are similar to those presented in Smedsrud et al. (2017) with regard to observed trends. Smedsrud et al. (2017) analyzed sea ice area transport across 79°N utilizing two methods to include manual vector analysis and cross-strait geostrophic wind calculations from mean sea level pressure, and showed no long-term trend in area transport from 1935-2014, and slightly positive trend from 1979-2014. I concur with that result, however, the annual sea ice area export of 884,151 km^2 from that study for 1979-2014 is 31% greater than the value of 673,205 km^2 calculated here.

Similarly, Zamani et al. (2019) examined sea ice area and volume transport across Fram Strait at 82°N for the period of 1990-2010 using the Max Planck Institute Ocean Model (MPIOM), and found a mean annual area export for that period of 860,000 km^2. Zamani et al. (2019) also

compared MPIOM results to the same NSIDC products I utilize here, and found and annual area flux of 647,000 km^2 using Polar Pathfinder data. This is only 4% lower than the mean annual area transport I calculated using the same data set with sea ice concentration included. The authors of that study assigned most of the uncertainty in satellite-derived fluxes to uncertainties in Polar Pathfinder drift observations. Zamani et al. (2019) also examined volume flux across 82°N using the same model and found the average monthly sea ice volume flux to be 277 km^3 per month. Over that same period, I calculated 75 km^3 per month.

Ricker et al. (2018) examined sea ice volume export through the Fram Strait for 2010-2017. The sea ice drift data sets they chose were the low-resolution sea ice drift from the Ocean and Sea Ice Satellite Application Facility (OSI SAF), scatterometer and brightness temperature measurements from Ifremer-CERSAT (Centre ERS d'Archivage et de Traitement), and NSIDC Polar Pathfinder vectors. Sea ice thickness data was from the Alfred Wegener Institute CryoSat2 product, and sea ice concentration was from the European Organisation for the Exploitation of Meteorological Satellites (EUMETSAT) Ocean and Sea Ice Satellite Application Facility. For a winter period defined as November – April, Ricker et al. (2018) found a minimum integrated volume flux for those months of 1250 km^3 and a maximum of 1910 km^3. Over that same period I calculated a maximum of 639 km^3 for one winter period and a minimum of 369 km , both on an order of magnitude lower than Ricker et al. (2018) results. In their own comparison to the NSIDC product, the Polar Pathfinder results are consistently the lowest by an average of 26%. Results presented in Ricker et al. (2018) for volume export through Fram Strait from 2010 to 2017 are a similar order of magnitude to results from Kwok et al. (2004) for the period of 1991-1999, Vinje et al. (1998) for the period of 1990-1996, and Spreen et al. (2009) for the period of 2003-2008.

After comparing my results with these studies, I consistently underestimate the area and volume transport of sea ice across Fram Strait because of a bias in the Polar Pathfinder data set

towards slower velocities, and because of a bias in the PIOMAS data set towards underestimating sea ice thickness, especially thick ice in wintertime. The studies mentioned in this section all rely on different forms of sea ice motion estimation that consistently estimate higher velocities than the Polar Pathfinder data, and none of them rely on PIOMAS thickness to calculate volume. In conclusion the PIOMAS and NSIDC data suggest lower area and volume export than other sources, and as such there is a possibility that my results are skewed towards underestimation. In any regard my data sources allowed for a comprehensive and consistent analysis of volume transport over the entire length of the sea ice remote sensing era (1979 to present) as opposed to the narrower time windows mentioned herein.

4.3 Warming Atlantic

Figure 23 shows warming sea surface temperature compared with declining sea ice area in the two boxes depicted in figure 23.a. Sea surface temperature (SST) values from ERA5 (described in chapter 2) were briefly examined off the west coast of Norway, which is a known pathway for Atlantic water into the Arctic. A spatial mean temperature in the red box shown in Figure 23.a was

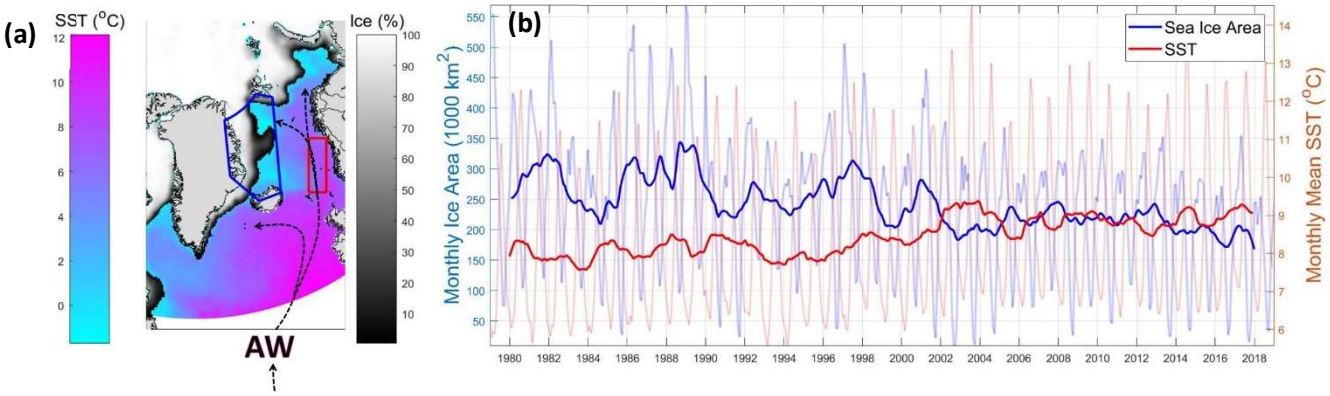

Figure 23. *(a) Sea ice concentration overlaid with sea surface temperature. Simplified branches of Atlantic Water Pathways are shown as black dashed lines. (b) Monthly sea ice area (left/blue) in the north box and monthly average sea surface temperature (right/red) in the red box on the west coast of Norway. Solid lines are 12-month running means.*

plotted monthly and compared to sea ice declining in the nearby north box of the study area. After detrending the two series shown, they are negatively correlated with a correlation coefficient of R= -0.78. This supports what is already an intuitive inverse relationship between warming water and sea ice.

Onarheim et al. (2014) examined the inflow of Atlantic water into Whaler's Bay, north of Svalbard using a moored hydrographic section in the West Spitsbergen Current which runs northward on the east side of the Fram Strait. They found that the shrinking winter sea ice cover was directly influenced by a core of warm Atlantic water between 1979 and 2012. Since the Odden Ice Tongue was directly to the west of the West Spitsbergen Current up until its disappearance, it is likely that increased heat flux towards the Odden from the inflow of Atlantic water contributed significantly to preventing it from forming after 2004.

Finally, Årthun and Eldevik (2016) examined poleward heat transport from the Atlantic to the Arctic using a 600-year control run of the Bergen Climate Model. They found that interannual and decadal ocean heat transport across the Greenland-Scotland Ridge propagate consistently toward the Arctic and explain variability in both SST and sea ice cover. They found a lag between the Greenland-Scotland inflow and the sea ice response of about 2 years, and using linear regression analysis they concluded that the simulated anomalous ocean heat transport predicts sea ice loss in the Greenland Sea Odden area with a reduction of 8% in sea ice concentration for one standard deviation in ocean heat transport (Årthun and Eldevik, 2016).

Based on these prior studies and the relationship shown here between sea surface temperature and sea ice area, I speculate that warming Atlantic waters (AW) are the primary driver behind the sea ice loss in the Greenland Sea, especially the loss of the Odden Ice Tongue.

CHAPTER 5: CONCLUSION

5.1 Conclusions

The results of this study are as follows:

1) Winter sea ice decline is much greater than summer sea ice decline in the Greenland Sea.
2) Sea ice are advected into the study area from the Artic has gone unchanged over the length of the satellite record.
3) Sea ice thickness across Fram Strait is on average 16% thinner after the disappearance of the Odden Ice Tongue.
4) Between 400 – 500 km^3 of sea ice is typically imported through Fram Strait over the course of a winter while less than 20 km^3 makes it down the coast and exits through the Denmark Strait. Approximately 40% of the ice that crosses Fram Strait melts over the course of the winter.

First, the decline of sea ice area in the Greenland Sea, Irminger Basin, and continental shelf of Greenland is much greater during the winter season than during the summer melting season. This trend is typical when compared to the Arctic as a whole, which has historically been experiencing the greatest sea ice loss during the summer minimum. This result agrees with similar previous studies. The largest relative contributor to sea ice loss is primarily the disappearance of the Odden Ice Tongue after 2004, which was typically characterized by local sea ice formation instead of sea ice advected into the area from the Arctic. Recent studies, some in progress, suggest that warming Atlantic Water is likely to blame for the loss of the Odden Ice Tongue.

Second, sea ice area advected into the Arctic has gone largely unchanged since the beginning of the satellite observation era beginning in late 1978. This also agrees with similar previous studies.

While the trend seen here is similar to other estimates of the sea ice area transport trend, the actual values of sea ice area transport produced here are significantly lower than the values presented the same previous studies. Comparison to those investigations suggests that sea ice motion estimates provided by the NSIDC are consistently less than other forms of direct observations of sea ice motion.

Third, sea ice thickness across Fram Strait is on average 16% thinner during the winter maximum after the disappearance of the Odden Ice Tongue than it was for 1979-2004. While there is no significant trend in values for monthly long-term volume flux (1979-2018), the seasonal integrated winter transport for the periods before and after 2004 decreased from 475 km^3 per winter to 421 km^3 per winter due to this thinning. These values are also significantly lower than similar studies because of likely bias in the PIOMAS thickness model to underestimate thick sea ice. This bias is combined with a bias in Polar Pathfinder sea ice motion vectors to underestimate sea ice motion, resulting in lower volume flux estimates.

The final result is a characterization of the typical sea ice volume budget for the winter in the Greenland Sea and continental shelf. Between 400 – 500 km^3 are typically imported through Fram Strait while less than 20 km^3 makes it down the coast and exits through the Denmark Strait. Estimates of the total change in sea ice volume over the winter (~250 km^3) made by applying a thickness to monthly area images are much smaller than the values of sea ice imported through the Fram Strait, meaning that approximately half of the sea ice that flows into the area must melt over the course of the winter. The Odden Ice Tongue contributed approximately 50 km^3 of sea ice volume to that seasonal volume change before its disappearance.

5.2 Future Work

A natural next step of this work would be a more thorough investigation into the driver(s) behind the sea ice loss trends in the study area. While I do posit here that warming Atlantic Water is likely the first order contributor, I did not examine changes in other relevant variables such as air temperature, climate indices like the North Atlantic Oscillation (NAO), or vertical/horizontal heat diffusion and ice/ocean interactions. A more complete assessment of the potential drivers could more clearly point to the likely cause of the trends in sea ice area and volume loss detailed here.

This thesis, in part is currently being prepared for submission for publication of the material. Straneo, Fiammetta; Smedsrud, Lars H. The thesis author was the primary investigator and author of this material.

REFERENCES

Årthun, M., & Eldevik, T. (2016). On Anomalous Ocean Heat Transport toward the Arctic and Associated Climate Predictability. *Journal of Climate*, *29*(2), 689–704. doi: 10.1175/jcli-d-15-0448.1

Cavalieri, D. J., Gloersen, P., & Campbell, W. J. (1984). Determination of sea ice parameters with the NIMBUS 7 SMMR. *Journal of Geophysical Research: Atmospheres*, *89*(D4), 5355–5369. doi: 10.1029/jd089id04p05355

Cavalieri, D. J., C. L. Parkinson, P. Gloersen, and H. J. Zwally. 1996, updated yearly. Sea Ice Concentrations from Nimbus-7 SMMR and DMSP SSM/I-SSMIS Passive Microwave Data, Version 1. Boulder, Colorado USA. NASA National Snow and Ice Data Center Distributed Active Archive Center. doi: https://doi.org/10.5067/8GQ8LZQVL0VL. 10 April 2019.

Comiso, J. C. (1986). Characteristics of Arctic winter sea ice from satellite multispectral microwave observations. *Journal of Geophysical Research*, *91*(C1), 975. doi: 10.1029/jc091ic01p00975

Comiso, J. C., Wadhams, P., Pedersen, L. T., & Gersten, R. A. (2001). Seasonal and interannual variability of the Odden ice tongue and a study of environmental effects. *Journal of Geophysical Research: Oceans*, *106*(C5), 9093–9116. doi: 10.1029/2000jc000204

Copernicus Climate Change Service (C3S) (2017): ERA5: Fifth generation of ECMWF atmospheric reanalyses of the global climate. Copernicus Climate Change Service Climate Data Store (CDS), 25 June 2019. https://cds.climate.copernicus.eu/cdsapp#!/home

de Steur, L., Pickart, R. S., Macrander, A., Våge, K., Harden, B., Jónsson, S., … Valdimarsson, H. (2017). Liquid freshwater transport estimates from the East Greenland Current based on continuous measurements north of Denmark Strait. *Journal of Geophysical Research: Oceans*, *122*(1), 93–109. doi: 10.1002/2016jc012106

Deser, C., Walsh, J. E., & Timlin, M. S. (2000). Arctic Sea Ice Variability in the Context of Recent Atmospheric Circulation Trends. *Journal of Climate*, *13*(3), 617–633. doi: 10.1175/1520-0442(2000)013<0617:asivit>2.0.co;2

Greene, Chad A., Gwyther D. E., Blankenship D. D. (2017). “Antarctic Mapping Tools for Matlab.” Computers & Geosciences, vol. 104, Elsevier BV, July 2017, pp. 151–57, doi:10.1016/j.cageo.2016.08.003.

Hansen, E., Gerland, S., Granskog, M. A., Pavlova, O., Renner, A. H. H., Haapala, J., … Tschudi, M. (2013). Thinning of Arctic sea ice observed in Fram Strait: 1990-2011. *Journal of Geophysical Research: Oceans*, *118*(10), 5202–5221. doi: 10.1002/jgrc.20393

IPCC: Climate Change 2007: The Physical Science Basis. Contribution of Working Group I to the Fourth Assessment Report of the Intergovernmental Panel on Climate Change, edited by: Solomon, S., Qin, D., Manning, M., Chen, Z., Marquis, M., Averyt, K. B., Tignor, M., and Miller, H. L., Cambridge University Press, Cambridge, United Kingdom and New York, NY, USA, 2007.

IPCC: Climate Change 2013: The Physical Science Basis. Contribution of Working Group I to the Fifth Assessment Report of the Intergovernmental Panel on Climate Change, edited by: Stocker, T. F., Qin, D., Plattner, G.-K., Tignor, M., Allen, S. K., Boschung, J., Nauels, A., Xia, Y., Bex, V., and Midgley, P. M., Cambridge University Press, Cambridge, United Kingdom and New York, NY, USA, 2013

Kwok, R. (2004). Fram Strait sea ice outflow. *Journal of Geophysical Research*, *109*(C1). doi: 10.1029/2003jc001785

Levitus, S. (2000). Warming of the World Ocean. *Science*, *287*(5461), 2225–2229. doi: 10.1126/science.287.5461.2225

Lindsay, R. (2010). New Unified Sea Ice Thickness Climate Data Record. *Eos, Transactions American Geophysical Union*, *91*(44), 405. doi: 10.1029/2010eo440001

Muilwijk, M., Smedsrud, L. H., Ilicak, M., & Drange, H. (2018). Atlantic Water Heat Transport Variability in the 20th Century Arctic Ocean From a Global Ocean Model and Observations. *Journal of Geophysical Research: Oceans*, *123*(11), 8159–8179. doi: 10.1029/2018jc014327

National Ice Center and National Snow and Ice Data Center. Compiled by F. Fetterer, M. Savoie, S. Helfrich, and P. Clemente-Colón. 2010, updated daily. Multisensor Analyzed Sea Ice Extent - Northern Hemisphere (MASIE-NH), Version 1. Boulder, Colorado USA. NSIDC: National Snow and Ice Data Center. doi: https://doi.org/10.7265/N5GT5K3K. 12/11/2019.

Onarheim, I. H., Smedsrud, L. H., Ingvaldsen, R. B., & Nilsen, F. (2014). Loss of sea ice during winter north of Svalbard. *Tellus A: Dynamic Meteorology and Oceanography*, *66*(1), 23933. doi: 10.3402/tellusa.v66.23933

Onarheim, I., Eldevik, T., & Smedsrud, L. H. (2018). Seasonal and regional manifestation of Arctic sea ice loss. *Journal of Climate*, *31*, 4917–4932. doi: 10.1175/JCLI-D-17-0427.1

Peng, G., Meier, W. N., Scott, D. J., Savoie, M. H., "A Long-Term and Reproducible Passive Microwave Sea Ice Concentration Data Record for Climate Studies and Monitoring." *Earth System Science Data*, vol. 5, no. 2, 2013, pp. 311–318., doi:10.5194/essd-5-311-2013.

Pistone, K., Eisenman, I., & Ramanathan, V. (2019). Radiative Heating of an Ice-Free Arctic Ocean. *Geophysical Research Letters*, *46*(13), 7474–7480. doi: 10.1029/2019gl082914

Ricker, R. (2018). Satellite-derived sea-ice export and its impact on Arctic ice mass balance. *The Cryosphere*, *12*, 3017–3032. doi: 10.5194/tc-2018-6-ac1

Schweiger, A., Lindsay, R., Zhang, J., Steele, M., Stern, H., & Kwok, R. (2011). Uncertainty in modeled Arctic sea ice volume. *Journal of Geophysical Research*, *116*. doi: 10.1029/2011jc007084

Shuchman, R. A., Josberger, E. G., Russel, C. A., Fischer, K. W., Johannessen, O. M., Johannessen, J., & Gloersen, P. (1998). Greenland Sea Odden sea ice feature: Intra-annual and interannual variability. *Journal of Geophysical Research: Oceans*, *103*(C6), 12709–12724. doi: 10.1029/98jc00375

Smedsrud, L. H. (2016). Fram Strait sea ice export variability and September Arctic sea ice extent over the last 80 years. *The Cryosphere*, *11*, 65–79. doi: 10.5194/tc-2016-79-ac2

Smedsrud, L. H. (2020) Nordic Cooling revisited - 100 years of service for the Global Ocean (In Preparation).

Smedsrud, L. H., Sorteberg, A., & Kloster, K. (2008). Recent and future changes of the Arctic sea-ice cover. Geophysical Research Letters, 35(20). doi: 10.1029/2008gl034813

Spielhagen, R. F., Werner, K., Sorensen, S. A., Zamelczyk, K., Kandiano, E., Budeus, G., Hald, M. (2011). Enhanced Modern Heat Transfer to the Arctic by Warm Atlantic Water. *Science*, *331*(6016), 450–453. doi: 10.1126/science.1197397

Spreen, G., Kern, S., Stammer, D., & Hansen, E. (2009). Fram Strait sea ice volume export estimated between 2003 and 2008 from satellite data. *Geophysical Research Letters*, *36*(19). doi: 10.1029/2009gl039591

Stroeve, J., & Notz, D. (2018). Changing state of Arctic sea ice across all seasons. *Environmental Research Letters*, *13*(10), 103001. doi: 10.1088/1748-9326/aade56

Talley, Lynne D., Pickard, George L., Emery, William J., Swift, James H., Physical Oceanography: An Introduction. 6th ed., Elsevier Academic Press, 2011.

Thorndike, A. S., & Colony, R. (1982). Sea ice motion in response to geostrophic winds. *Journal of Geophysical Research*, *87*(C8), 5845. doi: 10.1029/jc087ic08p05845

Toole, J. M., Timmermans, M.-L., Perovich, D. K., Krishfield, R. A., Proshutinsky, A., & Richter-Menge, J. A. (2010). Influences of the ocean surface mixed layer and thermohaline stratification on Arctic Sea ice in the central Canada Basin. *Journal of Geophysical Research*, *115*(C10). doi: 10.1029/2009jc005660

Tschudi, M., W. N. Meier, J. S. Stewart, C. Fowler, and J. Maslanik. 2019. Polar Pathfinder Daily 25 km EASE-Grid Sea Ice Motion Vectors, Version 4. Boulder, Colorado USA. NASA National Snow and Ice Data Center Distributed Active Archive Center. doi: https://doi.org/10.5067/INAWUWO7QH7B. 06 January 2020.

Vinje, T., Nordlund, N., & Kvambekk, Å. (1998). Monitoring ice thickness in Fram Strait. *Journal of Geophysical Research: Oceans*, *103*(C5), 10437–10449. doi: 10.1029/97jc03360

Våge, K., Pickart, R. S., Spall, M. A., Moore, G., Valdimarsson, H., Torres, D. J., … Nilsen, J. E. Ø. (2013). Revised circulation scheme north of the Denmark Strait. *Deep Sea Research Part I: Oceanographic Research Papers*, *79*, 20–39. doi: 10.1016/j.dsr.2013.05.007

Wadhams, P., & Comiso, J. (2000). Correction to "Two modes of appearance of the Odden Ice Tongue in the Greenland Sea." *Geophysical Research Letters*, *27*(5), 717–717. doi: 10.1029/2000gl000001

Wilkinson, J. P. (2006), Ice dynamics in the central Greenland Sea, J. Geophys. Res., 111, C12022, doi:10.1029/2006JC003639.

Zamani, B., Krumpen, T., Smedsrud, L. H., & Gerdes, R. (2019). Fram Strait sea ice export affected by thinning: comparing high-resolution simulations and observations. *Climate Dynamics*, *53*(5-6), 3257–3270. doi: 10.1007/s00382-019-04699-z

Zhang, J., & Rothrock, D. A. (2003). Modeling Global Sea Ice with a Thickness and Enthalpy Distribution Model in Generalized Curvilinear Coordinates. *Monthly Weather Review*, *131*(5), 845–861. doi: 10.1175/1520-0493(2003)131<0845:mgsiwa>2.0.co;2